# INVESTIGATION OF INTERFACES UNDER MECHANICAL AND THERMAL LOADING USING A COHESIVE ZONE MODEL

A Dissertation

by

ÖVÜL ÖZGÜ ÖZSOY

Submitted to the Office of Graduate and Professional Studies of
Texas A&M University
in partial fulfillment of the requirements for the degree of

DOCTOR OF PHILOSOPHY

| | |
|---|---|
| Chair of Committee, | Junuthula N. Reddy |
| Committee Members, | Ozden Ochoa |
| | Ibrahim Karaman |
| | Xin-Lin Gao |
| Head of Department, | Andreas A. Polycarpou |

May 2014

Major Subject: Mechanical Engineering

# ABSTRACT

Failures of structures is a great concern of engineering for longer and safer service life. The ability to predict a damage and failure depends on understanding the deformation and stress that develop in the material. Damage (microlevel failures) and failures often initiate at material interfaces. Interactions between different material phases, as well as crack initiation and propagation, make fracture and damage processes very difficult to analyze. The interfaces between dissimilar layers in the functionally graded hybrid material (FGHC) are the most critical for reliability. The use of different processes and materials to fabricate a hybrid material induce mismatch strains, making interfacial failure a primary damage mechanism. As advanced materials are introduced in load bearing structures in aerospace applications to improve performance, maintenance, and manufacturing, designing safe interfaces becomes a paramount goal. Creating seamless interfaces and mechanical locking between metal and polymer matrix composite layers is possible by fabricating a metal surface with various surface features. One of the joining methods is using carbon nanotube grown on the fabric surface, with the subsequent infusion of resin. This method makes use of grown forest of carbon nanotubes using carbon vapor deposition.

Experimental techniques are well established for determining interlaminar fracture in composite material systems. The mode I interlaminar fracture toughness can be obtained by the mode I test standard, which uses double cantilever beam specimen. Similarly, mode II and mixed-mode properties are extracted by designated test standards, such as end-notch flexure test and mixed mode bending test. Double cantilever beam test is conducted to explore fracture toughness of hybrid interfaces

modified by carbon nanotube grown on carbon fabric and Ti-foil as a function of temperature to assess its potential use within FGHC. It is seen that fracture toughness of modified interfaces in mode I is higher than the unmodified interfaces.

In the present study, computational assessment of joining a metal laminate to carbon fiber reinforced polymer (CFRP) laminate was undertaken to investigate interlaminar response and mode I and II delamination toughness. The objective of the present research was to develop a computational model to study delamination in laminated composite plates subjected to bending and extensional loads, and to study different joining techniques, as well as to predict the thermomechanical interfacial response. This model incorporates extreme environment conditions, such as high temperature to study these joining techniques. Experimental data of DCB tests were obtained in collaboration with Dr. Ochoa's group in order to validate and verify the computational solutions.

The results of this study are expected to provide a better understanding of interface mechanical behavior, thereby provide both materials scientists and designers in selecting alternate material systems and interfaces so that enhanced structural properties such as interfacial strength and durability of the joints subject to out-of-plane bending, impact, and fatigue loading are realized.

To my family

# ACKNOWLEDGEMENTS

Firstly, I would like to express my sincere gratitude to my advisor Prof. Dr. J.N. Reddy for offering me his full support and encouragement throughout the course of this research, for his patience and time throughout my Ph.D. study. He has been a source of inspiration and will always be.

I am grateful to Prof. Dr. Ozden Ochoa, who started this journey, supported me from the very beginning of my study, constantly watched over my progress. Our collaboration and their experimental support helped the progress of this research.

I am thankful to my committee members, Prof. Dr. Ibrahim Karaman and Prof. Dr. Xin-Lin Gao for their support and their valuable comments on this work.

The assistance and support and friendship of all members of the ACML(Advanced Computational Mechanics Laboratory) and MURI team were greatly appreciated.

I would like to thank to AFOSR MURI Grant FA9550-09-1-0686 for the sponsorship for this research.

There are no words that could express my gratitude for the love and encouragement of my family during my entire life. I will always be grateful for their unconditional support. Without them, this dissertation would not have been written.

# NOMENCLATURE

| | |
|---|---|
| CNT | Carbon Nano Fiber |
| CTE | Coefficient of Thermal Mismatch |
| CZM | Cohesive Zone Model |
| DCB | Double Cantilever Beam |
| DCJ | Double Cantilever Joint |
| ENF | End Notch Flexure |
| FGHC | Functionally Graded Hybrid Composies |
| HTCL | Hybrid Titanium Composite Laminates |
| SLJ | Single Lap Joint |
| SLS | Single Lap Shear |
| $\delta$ | Displacement |
| $\Delta$ | Crack opening widths |
| $\sigma$ | Stress |
| $\varepsilon$ | Strain |
| $\mu$ | Frictional coefficient |
| $\Psi$ | Potential |
| $G_I, G_{II}, G_{III}$ | Strain Energy Release Rates for mode I, II, and III |
| $G_{Ic}, G_{IIc}, G_{IIIc}$ | Critical Strain Energy Release Rates for mode I, II, and III |
| $K$ | Stiffness Matrix |
| $S$ | Material Tangent Matrix |
| $t$ | Traction |
| subscript $n$ | normal direction |
| subscript $t$ | tangential direction |

TABLE OF CONTENTS

LIST OF FIGURES

FIGURE Page

LIST OF TABLES

TABLE Page

# 1. INTRODUCTION

Polymers can be used to bond structural parts with similar or different materials together. Polymeric joints have several advantages over other types of methods such as bolts, rivets or welding. A well-known issue with these joining systems is the creation of high stress concentration areas. Also, polymeric joints are light-weight compared to them, which increase their importance especially in aerospace and automotive industries. They also have better damping and fatigue characteristics.

Titanium graphite (TiGr) also known as Hybrid Titanium Composite Laminates (HTCL) consist of a carbon fiber reinforced polymer sandwiched between metal laminates. It is developed to be used mostly in aircrafts for high temperature applications. However the interfaces between dissimilar layers are critical regions for failure in thermal and mechanical loadings due to mismatch in the strains.

## 1.1 Overview of Cohesive Zone Model

Failure in materials can be simulated by several methods such as fracture mechanics, continuum damage mechanics and XFEM. Fracture can be evaluated carefully depending on where, and at which scale it occurs. Fracture mechanics and continuum damage mechanics are not suitable for every fracture behavior. Cohesive zone theory is another method, which overcomes the restrictions by the aforementioned methods, such that it can be suitable for both crack initiation and growth. It can be executed in finite element, as well. The first discussions of cohesive zone models (CZM) were made in the works of Dugdale [1] and Barenblatt [2]. In CZMs, crack initiation and propagation can be calculated for both ductile and brittle materials. Cohesive zone model can be used to analyze both linear and nonlinear fracture process such as void growth and microcrack. [1, 2, 3].

In a cohesive zone model, the process of the fracture can be investigated in four regions (Fig. 1.1).

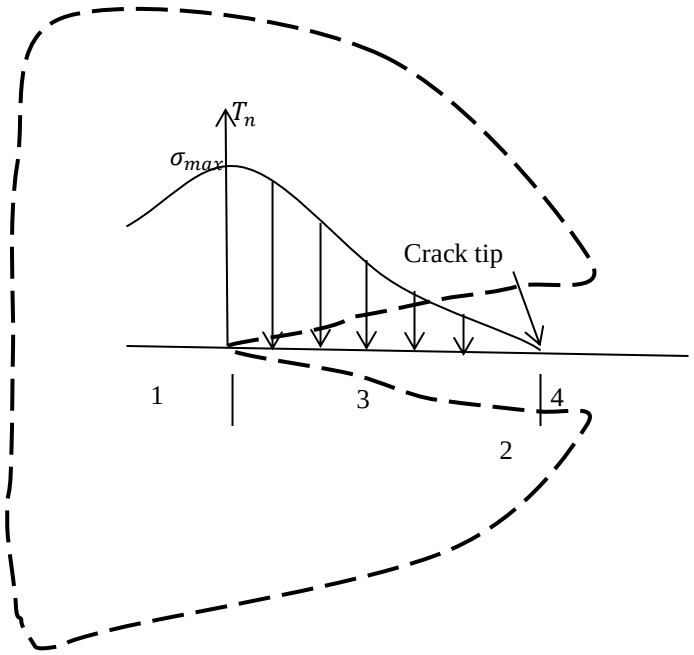


Figure 1.1: Schematics of the cohesive zone model

Initially, there is no fracture and the material behaves as continuum (Region 1) in 1.1). In Region 2, crack initiates based on a failure criterium. There are several criteria mentioned in the literature, such as maximum stress [4] , maximum strain [5], minimum strain energy density [6], or loss of ellipticity [7]. After the damage

initiates based on one of these criteria, the crack continue to grow (3). At this step, the material behaves with respect to the interaction of tractions arised during fracture at the surfaces and separations along the crack. The part of the curve during damage evolution is related to the fracture process behavior. Hence, the traction-separation relation can fully represent the whole fracture process. Damage evolution part can be described as a linear softening model, which is more suitable for brittle type of failure [8], or as a trapezoidal curve, which is useful to define an elastic-plastic solid [9].Van den Bosch et al. [10] also used a trapezoidal traction-separation relation an exponential relationship under mixed mode conditions by improving the description of Xu and Needleman [11]. When the crack opening reaches to its maximum value, then the materials fails, This falls in the forth region (4), where the material can no longer carry loads;i.e. there is no traction.

The fracture progressively develops in cohesive zone models . As the crack opens, cohesive tractions resist the separation[12]. Cohesive elements used in finite element defines those tractions during crack, which uses traction-separation constitutive behavior instead of the physical material properties.

The simulation of crack can be achieved by cohesive zone elements. Since cohesive elements are placed along the crack path, crack cannot follow another direction. This brings mesh-dependency. Because of that, the mesh should be carefully examined and refined. There exist both normal and shear tractions, which are along the crack and across the crack, respectively. As mentioned earlier, traction is a function of separation, which can fully describe failure behavior. There are several traction-separation laws [13], but the overall response of the material remains the same regardless of the selected traction-separation law. During the propagation of a crack, tractions increase until they reach a critical point, where damage initiates. After the initiation, traction drops to zero, followed by the complete failure (complete

separation of the surfaces). The area under the curve gives the fracture energy, as the maximum value of the traction corresponds to interface strength. Characterization of cohesive interface properties is the most challenging park in applying the cohesive zone model a failure analysis at that interface. The constitutive relation in cohesive zone models can be derived from a potential function [14, 15, 11]. Also other types of derivations of the constitutive relations can be found in literature [16, 17, 18, 19, 10].

Cohesive zone theory can be employed in multi-scale framework in heterogeneous adhesives [20, 21, 22]. In general, if there exist a function such that its gradient is a vector field, then this function is called as a potential function. Therefore, it can be used to represent any physical field such as strain energy, which can be used to obtain stress distributions. If it is applied to the fracture energy, the first derivative of the potential function gives the traction, and the second derivative of it provides the constitutive relationship.

Potential functions can be selected differently for a cohesive zone. They can be exponential, polynomial or periodic. First a polynomial, later an exponential-periodic function is studied by Needleman [14, 23], to investigate large shear displacements.

The main drawback of the potential function used by Tvergaard and Hutchinson [15] is that it assumes the fracture energies for mode I and II are equal, however, it works well in simulating the fracture behavior.It is important to be able to define different fracture energies for each mode for most of the materials [5]. It has been shown that the fracture energy changes in mode I and II through several tests [24, 25, 26].

A mixed-mode fracture is simulated in an adhesive joint which deforms plastically by a non-potential cohesive zone model [17]. Zhang and Paulino [19] presented a dynamic analysis in functionally graded materials, and defined the traction-separation relationship as bilinear.

Rose [27] defined the normal interaction by an exponential function and Rice [28] used a the a periodic function to represent tangential interaction. Xu and Needleman [11] also used exponential function for both normal and tangential and they took failure due to shear into account.

Gurtin [29] presented a detailed thermodynamic analysis of the cohesive zone in a growing crack. Fagerström and Larsson [30] extended the cohesive zone by considering heat generation and energy transport between the fracture surfaces. Thermal conduction due to bridging fibers and mechanical effects are coupled in Hattiangadi and Siegmund [31]. They also considered heat radiation in the gap exists in fractured region, as well as the heat flux by the gas trapped in this gap. Benabou et al. [32] predicted the lifetime for solder joints, considering conductance of the cohesive zone under fatigue loading. Nikalova and Ivanova [33] employed a shear lag model to provide an analytical solution for debonding in bi-material plates subjected to thermomechnical loading. Adhesively bonded joints can be subjected to cyclic thermal loads,which has a degrading effect on the adhesive [34].

## 1.2 Single Lap Shear Modeling

The most common method to obtain shear strength of the interface in adhesively bonded joint is the lap shear test. There are different kinds of lap shear tests, such as single lap shear and double lap shear. In a lap joint, usually, the tensile stresses develop over the entire joint and shear stresses are observed mainly across the bonded area. This is because the adherents force to slide over each other. In a lap shear test, one end is fixed, and a tensional force is applied at the other end. However, due to eccentricity of the load in a single lap shear, in addition to shear stresses, peel stresses develop, and the stresses along the overlap length are not uniform. Goland and Reissner [35] introduced the eccentricity for the first time and solved analytically

and discussed its effects in detail. The stress concentrates towards the ends of the overlap region, which is the main cause for debonding to initiate and propagate at the ends. Hence, the stresses at the ends plays the most important role in lap shear joints. Shear deformations and bending of the adherents, as well as adhesive thickness can affect the strength in two-dimensional SLJ and double lap joint (DLJ) models with similar metal adherents [36]. Adams and Peppiatt [36] made a plane-strain assumption and used triangular finite elements. Their finite element results showed close agreement with analytical solutions. A strain-displacement equation can represent the behavior of the adhesive layer, and the adhesive thickness is more effective as the length of the overlap decreases. [35, 37, 38]. Carpenter's finite element analysis [38] based on the previous works [35, 37].

The adhesive material can be considered as linear-elastic, elastic-plastic or viscoelastic, depending on the polymer properties or operation temperatures. Also, adherents can be made of similar or different materials, as well as they may have different thicknesses. These geometric and material properties can significantly effect the strength prediction of the joint. Adherents may be isotropic or orthotropic materials, as well as considered as plates or beams. However, if they are modeled as plate a shear deformation theory is used.

Another important component of lap joint analysis is boundary condition at the ends of the joint. Reddy and Roy [39] showed their effects in a detailed analysis and assumed elastic solids and represented them by an updated Lagrangian formulation. Geometric nonlinearity is included in their two-dimensional finite element analysis.

An explicit closed-form solution is provided by Zhao et al. [40, 41] for the elastic stress analysis in SLJs. This solution helped to predict zero shear stress at the free ends of the adhesive. Also, the normal stress varied through the thickness of the adhesive. They conducted a parametric study to show the effects of different thicknesses

and dissimilar materials for adherents and compared their finite element results for a two dimensional and geometrically nonlinear with Bigwood and Crocombe's [42] theoretical solution. They found that the peel stresses along the centerline of the adhesive are lower in the thicker adhesive, and the maximum normal stresses and strains lie between the centerline and the adhesive-adherend interface. However, in conclusions they reported their results incorrectly as saying that the thicker the adhesive bond layer, the higher the magnitude of the peel stresses and strains thus the larger the bending deformation. They also proposed a methodology to treat the cohesive failure in the adhesive layer and possible failure mechanisms. Magalhaes et al. [43] found that the maximum stresses develop at both interfaces between adhesive and adherents, at two ends of the adhesive bond. This result supports the previous comments on critical regions for damage initiation. An elastic-perfectly plastic adhesive assumption may be better to obtain the joint strength for investigating cohesive behavior in the fracture process [44]. Cooper and Sawyer [45] tried to obtain stresses. They developed equations with a plate behavior,which is assumed consistent throughout the development. In addition, small terms retained for a more complete solution.

If the thickness of the adhesive very small than that of the adherents, stress variations across its thickness can be neglected [46]. Another example with orthotropic adherents are composite materials used in the work of Li et al. [47]. He analysed stress-strain distributions in the thickness direction of the adhesive with a nonlinear finite element model. They found that as the adhesive gets thicker, the peel stresses in the adhesive layer decreases. The maximum normal stresses and strains shift towards to the adhesive-adherend interface. However, they reported their results incorrectly as saying that the thicker the adhesive bond layer, the higher is the magnitude of the peel stresses and strains thus bending deformation is larger.

## 1.3 Double Cantilever Beam Modeling

The double cantilever beam is the most commonly used method to obtain mode I fracture properties, whereas end notch flexure test is useful for mode II fracture properties. Cohesive zone properties are difficult to define, and an inverse method helps to get required properties from the test data.

Alfano and Crielsfield [48] used interface elements and damage law in their finite element analysis to model delamination in laminated composite plates. He modified the mixed mode formulation to avoid inconsistencies. De Moura et al. [49] compared continuum damage models with cohesive damage models. In his work, cohesive damage model comprises the ductile behavior of the interface. A continuum mixed-mode damage model was also developed to evaluate the mechanical influence of adhesive thickness on fracture energy. Xie and Waas [50] used a discrete cohesive zone model to simulate crack initiation and propagation, considering non-linear effects of the material. It can be implemented using beam elements. They reported insensitivity to the mesh size and the load increment, which possibly is responsible for a reduced computation time compared to existing cohesive zone models when it is utilized through a user subroutine UMAT in ABAQUS. Roe and Sigmund [51] studied a cohesive zone model for fatigue crack growth, which is described by an irreversible constitutive equation for the cyclic interface traction-separation relationship. The traction-separation path is usually is not predefined on the contrary to previous models. The separation behavior changes at different material points. De Moura and Chousal [52]applied the cohesive model with a linear softening behavior to simulate a double cantilever beam and end notch flexure tests. The model was found to be more successful for mode I than it was for mode II due to the assumptions made to simplify hte cohesive zone model. Tenchev and Falzon [53] conducted experiments

to characterize the interface fracture properties in mode I and mode II, and showed that a non-linear softening relation more accurate results than the linear one.

Crisfield and Davies [54] studied delamination in a DCB model with a proposed cohesive method, which requires a nonlinear FE software and "adaptive mesh" ability. and showed that mesh density highly affects the solutions. Harper and Hallett [55] also paid attention to the mesh density and required number of elements to accurately analyze the delamination in composites, and observed values of interfacial strength. A cohesive zone element was introduced and implemented in finite element explicitly by Pinho et al. [56]. Turon et al. [57, 58] determined the constitutive parameters for a delamination problem by applying a methodology. They studied the effect of the cohesive element length, cohesive zone length and the maximum traction strength. Another important parameter, penalty stiffness, is estimated by a closed-form solution. Diehl [59, 60] presented a penalty methodology that enables the use of CZM where the critical energy release rate, $G_c$ is the only known property of the interface. Goyal et al. [61] simplified the strength criteria by introducing a elements with an irreversible constitutive relation.

## 1.4 Objectives

The objective of the proposed research is to develop a computational model to study delaminations in laminated composite plates subjected to bending and extensional loads, as well as to design and predict the thermo-mechanical interfacial response. A potential-based cohesive theory is used to model the interfaces. This model is incorporated extreme environment conditions such as high temperature to study these joining techniques.

## 1.5 Approach

In the present study, computational assessment of joining a metal laminate to carbon fiber reinforced polymer (CFRP) laminate is undertaken to investigate interlaminar response and mode I and II delamination toughness. The plan is to study different joining techniques to facilitate mechanical locking with the CFRP layer. Experimental data of double cantilever beam (DCB) tests are obtained in collaboration with Dr. O. Ochoa's group in order to validate and verify the computational solutions.

# 2. COHESIVE ZONE THEORY AND CONSTITUTIVE RELATIONSHIPS

## 2.1 Traction-Separation Law

Traction-separation law is used to define the constitutive behavior of the material. Figure 2.1 shows a typical traction and separation relationship. Here, $t_{max}$ can be the maximum traction in normal, shear or transverse directions ($t_n, t_s$ and $t_t$). Normal direction means normal to the fracture surface, whereas the remain two represent traction components parallel to the fracture surface. Damage initiates when the traction increases to a maximum when the displacement reaches a critical opening of the crack. K is an artificial stiffness that relates traction to displacement for the elastic region. Damage evolution region (softening region) follows the elastic region after damage initiates.

When one can obtain only the critical energy release rate through the tests, it becomes challenging to characterize the interface. Traction-separation law and force displacement curve help to identify the required parameters to define the cohesive interface properties. the The determination of the cohesive zone properties are based on ad-hod relations, so that it is difficult to create general results. ABAQUS software provides a cohesive element called COH4D2. These elements have four nodes with two translational degrees of freedom per node.

### *2.1.1 Damage Initiation and Progressive Failure*

When the traction reaches to a maximum, damage initiates and material stiffness starts to degrade. Maximum quadratic nominal stress or strain criteria can be written as

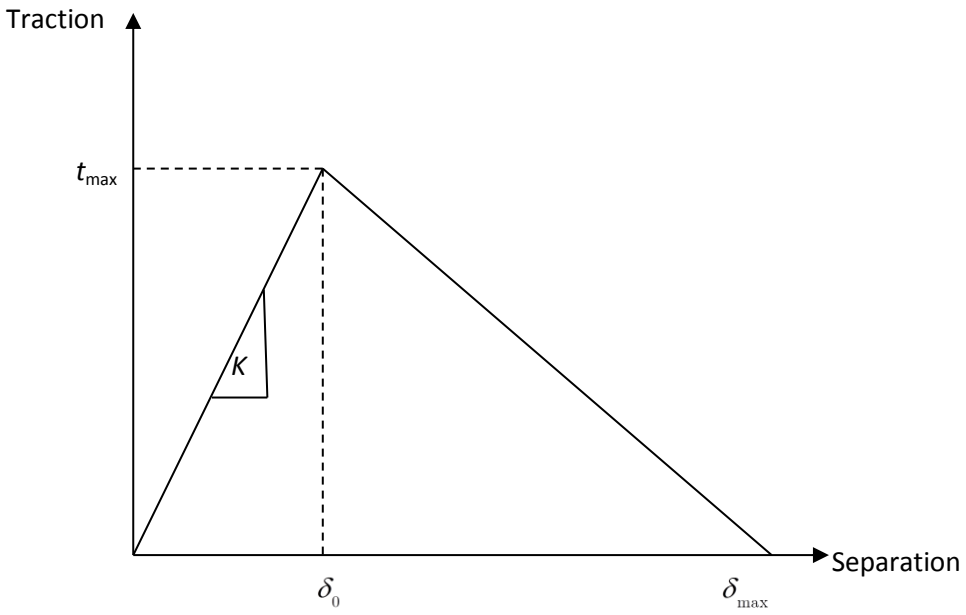


Figure 2.1: Traction-separation constitutive response

$$MAX\left\{\frac{\sigma_n}{\sigma_{n_max}}, \frac{\sigma_s}{\sigma_{s_max}}, \frac{\sigma_t}{\sigma_{t_max}}\right\} = 1, \left(MAX\left\{\frac{\varepsilon_n}{\varepsilon_n^{max}}, \frac{\varepsilon_s}{\varepsilon_s^{max}}, \frac{\varepsilon_t}{\varepsilon_t^{max}}\right\} = 1\right) \tag{2.1}$$

or quadratic nominal stress (strain) criterion,

$$\left(\frac{\sigma_n}{\sigma_{n_max}}\right)^2 + \left(\frac{\sigma_s}{\sigma_{s_max}}\right)^2 + \left(\frac{\sigma_t}{\sigma_{t_max}}\right)^2 = 1, \left(\left(\frac{\varepsilon_n}{\varepsilon_n^{max}}\right)^2 + \left(\frac{\varepsilon_s}{\varepsilon_s^{max}}\right)^2 + \left(\frac{\varepsilon_t}{\varepsilon_t^{max}}\right)^2 = 1\right) \tag{2.2}$$

where $\sigma_{n_max}, \sigma_{s_max}, \sigma_{t_max}$, and for strain $(\varepsilon_n^{max}, \varepsilon_s^{max}, \varepsilon_t^{max})$ are the maximum stress and maximum strain values, respectively.

Damage progresses after the initiation with continuing degradation of the material stiffness. The rate of degradation can be described in terms of fracture energy.

Benzeggagh-Kenane (BK) expression 2.3 [26] can be used to define the fracture energy as a function of mixed-mode .

$$\begin{aligned} &G_{IC} + (G_{IIC} - G_{IC}) \left(\frac{G_{shear}}{G_T}\right)^{\eta} = G_{TC} \\ &G_{shear} = G_{II} + G_{III} \\ &G_T = G_I + G_{shear} \end{aligned} \tag{2.3}$$

or Power law as given below,

$$\left(\frac{G_I}{G_{IC}}\right)^{a} + \left(\frac{G_{II}}{G_{IIC}}\right)^{a} + \left(\frac{G_{III}}{G_{IIIC}}\right)^{a} = 1 \tag{2.4}$$

where $G_{IC}, G_{IIC}, G_{IIIC}$ are the critical strain energy release rates for mode I, II, and III, respectively. The expressions 2.3 and 2.4 are empirically found expressions by fitting the force-displacement results.

## 2.2 Cohesive Zone Model and Derivation of Cohesive Properties Using a Potential Function

As discussed previously, unified potential-based cohesive zone model is implemented in a finite element model through a user-defined element subroutine in ABAQUS software be Park et al. [62]. This two-dimensional linear cohesive element will be extended to study laminated composite plates subjected to bending and extensional loads. The most challenging part of applying a cohesive zone model for fracture analyses at an interface is finding the interface fracture properties. One need to define nine parameters in order to use the discussed model, i.e. fracture energy for mode I and mode I, normal and tangential interface strength, a parameter to control the softening behavior of the material and a slope parameter to define the elastic region up to damage initiation. Also, one need to input the thickness of the interface element (the thickness of the interface between the two surfaces.). Traction can be found as a function of separation using the potential function, so that one can obtain a relationship between the two.

The potential function used in [63] is given by

$$\begin{aligned}\Psi\left(\Delta_n, \Delta_t\right) = min\left(G_I, G_{II}\right) + \left[\mathrm{r}_n\left(1 - \frac{\Delta_n}{\delta_n}\right)^a \left(\frac{k}{a} + \frac{\Delta_n}{\delta_n}\right)^k + G_I - G_{II}\right] \\ \left[\mathrm{r}_t\left(1 - \frac{|\Delta_t|}{\delta_t}\right)^b \left(\frac{l}{b} + \frac{|\Delta_t|}{\delta_t}\right)^l + G_{II} - G_I\right]\end{aligned} \tag{2.5}$$

and $\langle\cdot\rangle$ (the Macauley bracket)used above, has the following properties.

$$x = \begin{cases} 0, x \leq 0 \\ x, x > 0 \end{cases} \tag{2.6}$$

Normal and tangential tractions are the first derivatives of the potential function with respect to the separations in opening and shear modes, respectively [63].

$$t_n\left(\Delta_n,\Delta_t\right)=\frac{\mathrm{r}_n}{\delta_n}\left[\mathrm{k}\left(1-\frac{\Delta_n}{\delta_n}\right)^a\left(\frac{k}{a}+\frac{\Delta_n}{\delta_n}\right)^{k-1}-\mathrm{a}\left(1-\frac{\Delta_n}{\delta_n}\right)^{a-1}\left(\frac{k}{a}+\frac{\Delta_n}{\delta_n}\right)^{k}\right]\left[\mathrm{r}_t\left(1-\frac{|\Delta_t|}{\delta_t}\right)^b\left(\frac{k}{a}+\frac{|\Delta_t|}{\delta_n}\right)^{l}+G_{II}-G_I\right] \tag{2.7a}$$

$$t_t\left(\Delta_n,\Delta_t\right)=\frac{\mathrm{r}_t}{\delta_t}\left[\mathrm{l}\left(1-\frac{|\Delta_t|}{\delta_t}\right)^b\left(\frac{l}{b}+\frac{|\Delta_t|}{\delta_t}\right)^{l-1}-\mathrm{b}\left(1-\frac{|\Delta_t|}{\delta_t}\right)^{b-1}\left(\frac{l}{b}+\frac{|\Delta_t|}{\delta_t}\right)^{l}\right]\left[\mathrm{r}_n\left(1-\frac{\Delta_n}{\delta_n}\right)^a\left(\frac{k}{a}+\frac{\Delta_n}{\delta_n}\right)^{k}+G_I-G_{II}\right]\frac{\Delta_n}{|\Delta_t|} \tag{2.7b}$$

Here, m and n are nondimensional constants and defined as follows.

$$\begin{aligned} k&=\frac{a(a-1)\lambda_n^2}{(1-a\lambda_n^2)}\\ l&=\frac{b(b-1)\lambda_t^2}{(1-b\lambda_t^2)}\end{aligned} \tag{2.8}$$

$r_n$ and $r_n$ are also constants and related to the mode I and mode II fracture energies, respectively.

These equations provide very useful information about the boundary conditions, which can fully define the fracture characteristics [62].

If the partial derivatives of the function of normal and tangential tractions are taken with respect to the normal and tangential separations, one can find the maximum, which corresponds to the interface strength. The separation at which the function has maximum corresponds to the critical separation (or opening) for the

crack.

Mode I and mode II fracture energy $(G_I, G_{II})$ is equal to the area under the traction-separation curve for normal and tangential directions, respectively.

$$G_I = \int_0^{\delta_n} T_n\left(\Delta_n, 0\right) d\Delta_n, \quad G_{II} = \int_0^{\delta_t} T_t\left(0, \Delta_t\right) d\Delta_t \tag{2.9}$$

When we look at the equations above, we see that when the separation reaches to the critical crack opening, then traction becomes zero $(t_n = 0)$. This means that crack opened fully so that it does not carry any traction. The same applies for tangential traction as well $(t_t = 0)$.

Material response after damage initiates can be controlled by the shape parameters $(a, b)$. Taking values less equal or higher than two can change the damage evolution part of the curve from concave to convex shape, which determines whether the material will behave brittle or ductile.

Both normal and tangential components crack separation and constant can be found by applying the boundary conditions. The ratio of the critical crack opening width to the final crack opening width indicates the initial slope for the elastic region [62], given below.

$$\lambda_n = \delta_{nc}/\delta_n \qquad \lambda_t = \delta_{tc}/\delta_t \tag{2.10}$$

where $\delta_n, \delta_t$ are crack openings at initiation and $\delta_{nc}, \delta_{tc}$ are crack openings at failure. This is equivalent to K artificial stiffness in ABAQUS, in the sense that they both control the elastic region. As K gets higher values the initial stiffness increases, whereas in potential model the description of the initial slope ratio dictates that the slope is higher with the lower initial slope ratio.

### *2.2.1 Constitutive Behavior*

The constitutive relation of the mentioned potential-based model has been evaluated for loading (damage initiation and evolution), contact and failure conditions. The damage initiation and evolution takes place before the complete failure. The structure can be unloaded or reloaded as long as the traction does not exceed the maximum, where damage initiates. The crack surfaces are in contact until crack separates completely [64].

Contact condition is when the normal separation is negative, which means there exists penetration. To prevent the material penetration at the interface, negative normal separation is penalized, so that the tangential cohesive interaction is evaluated by mandating $\Delta_n = 0$.

The complete failure occurs when separations exceed the critical separations. In that case $\hat{t}_n$ ( normal stiffness) becomes zero. As the first derivative of the potential function gives the tractions,its vector can be shown as

$$\hat{t} = \left\{ \begin{array}{c} \partial\Psi/\partial\Delta_1 \\ \partial\Psi/\partial\Delta_2 \end{array} \right\} = \left\{ \begin{array}{c} \hat{t}_1 \\ \hat{t}_2 \end{array} \right\} \tag{2.11}$$

whereas the second derivative of the potential provides the material tangent matrix,

$$S(\Delta_n, \Delta_t) = \left[ \begin{array}{cc} S_{nn} & S_{nt} \\ S_{tn} & S_{tt} \end{array} \right] = \left[ \begin{array}{cc} \partial^2\Psi/\partial\Delta_n^2 & \partial^2\Psi/\partial\Delta_n\partial\Delta_t \\ \partial^2\Psi/\partial\Delta_t\partial\Delta_n & \partial^2\Psi/\partial\Delta_t^2 \end{array} \right] \tag{2.12}$$

the components of the tangent stiffness matrix in softening condition matrix are,

$$
\begin{aligned}
S_{nn} &= \frac{r_n}{\delta_n^2}\Bigg[(k^2-k)\left(1-\frac{\Delta_n}{\delta_n}\right)^a\left(\frac{k}{a}+\frac{\Delta_n}{\delta_n}\right)^{k-2}+(a^2-a)\left(1-\frac{\Delta_n}{\delta_n}\right)^{a-2}\left(\frac{k}{a}+\frac{\Delta_n}{\delta_n}\right)^{k} \\
&\quad -2ak\left(1-\frac{\Delta_n}{\delta_n}\right)^{a-1}\left(\frac{k}{a}+\frac{\Delta_n}{\delta_n}\right)^{k-1}\Bigg]\Bigg[r_t\left(1-\frac{\Delta_t}{\delta_t}\right)^b\left(\frac{l}{b}+\frac{\Delta_t}{\delta_t}\right)^l+\langle G_{II}-G_I\rangle\Bigg] \\
S_{nt} &= \frac{r_n r_t}{\delta_n\delta_t}\Bigg[k\left(1-\frac{\Delta_n}{\delta_n}\right)^a\left(\frac{k}{a}+\frac{\Delta_n}{\delta_n}\right)^{k-1}-a\left(1-\frac{\Delta_n}{\delta_n}\right)^{a-1}\left(\frac{k}{a}+\frac{\Delta_n}{\delta_n}\right)^{k}\Bigg] \\
&\quad \Bigg[l\left(1-\frac{\Delta_t}{\delta_t}\right)^b\left(\frac{l}{b}+\frac{\Delta_t}{\delta_t}\right)^{l-1}-b\left(1-\frac{\Delta_t}{\delta_t}\right)^{b-1}\left(\frac{l}{b}+\frac{\Delta_t}{\delta_t}\right)^{l}\Bigg] \\
S_{tn} &= 0 \\
S_{tt} &= \frac{r_t}{\delta_t^2}\Bigg[(l^2-l)\left(1-\frac{\Delta_t}{\delta_t}\right)^a\left(\frac{l}{b}+\frac{\Delta_t}{\delta_t}\right)^{l-2}+(b^2-b)\left(1-\frac{\Delta_t}{\delta_t}\right)^{b-2}\left(\frac{l}{b}+\frac{\Delta_n}{\delta_n}\right)^{l} \\
&\quad -2bl\left(1-\frac{\Delta_t}{\delta_t}\right)^{b-1}\left(\frac{l}{b}+\frac{\Delta_t}{\delta_t}\right)^{l-1}\Bigg]\Bigg[r_n\left(1-\frac{\Delta_n}{\delta_n}\right)^a\left(\frac{k}{a}+\frac{\Delta_n}{\delta_n}\right)^{k}+\langle G_I-G_{II}\rangle\Bigg]
\end{aligned}
\tag{2.13}
$$

as given in [64].

### *2.2.2 Extensions to the Potential-Based CZM for Friction and Thermal Expansion*

CZM is a useful method and can be improved by considering details of the fracture process. Other than different loading conditions such as fatigue, interaction between fracture surfaces is another point to pay attention. Contact condition of the fracture process can further be evaluated by considering frictional effects between fracture surfaces. Potential-based cohesive model [63] explained earlier can be modified to be able to capture friction. For contact condition, frictional sliding can be governed by Coulomb friction law. When the friction is included, cohesive tractions (normal and tangential) and cohesive displacement jumps (normal and tangential) are related as shown by Lin et al [65].

$$T_t = sign(\Delta_t)\mu T_n \tag{2.14}$$

for $|T_t| < \mu T_n$ for $\delta_n = 0$ condition, where $\mu$ is a constant friction coefficient [65]. Kuhn-Tucker conditions for Coulomb friction are given as in (2.15) [65].

$$\begin{aligned} &\phi = |T_t| - \mu|T_n| \leq 0 \\ &\dot{u}_t = \xi \tfrac{\partial}{\partial T_t}\Phi \\ &\xi \geq 0 \\ &\xi\Phi = 0 \end{aligned} \tag{2.15}$$

$\dot{u}_t = \xi \frac{\partial}{\partial T_t}\Phi$ and $\xi \geq 0$ dictates the sliding and applied shear traction is in opposite directions and slip will occur only when $\Phi = 0$ ($|T_t| = \mu|T_n|$). There is no slip when $|T_t| \leq \mu|T_n|$ ($\dot{u}_t = 0$).

Thermal residual stress is a big concern for composite materials. Residual stresses can initially develop by both chemical shrinkage of the resin and and CTE mismatch. Furthermore, structures operating at elevated temperatures are subjected to thermal loads.

A correction is proposed here for the crack opening at the interface due to thermal expansion of the interface material. In a polymer matrix fiber reinforced composite material, the fiber elongates or shortens due to thermal expansion and temperature difference, which may affect crack opening due to mechanical loading only. To this purpose, crack openings can be restated as shown in Equation set 2.16 [66] in two components for thermal and mechanical loading [66].

$$\begin{aligned} \Delta_n^T &= a_{int}\Delta\theta\Delta_n \\ \Delta_t^T &= a_{int}\Delta\theta\Delta_t \end{aligned} \tag{2.16}$$

Equation set 2.16 represent the tangential openings due to temperature,where mechanical crack openings are modified to take thermal expansion of the interface into account. Here, $\alpha_{int}$ is coefficient of the thermal expansion (CTE) of an interface where crack lies. $\alpha_{int}$ is a broad representative value, including not only CTE of the fiber but also the collective response of many crack bridging agents, their geometric arrangement and volumetric fraction of a heterogeneous interface [66].

Traction ($t_n$ and $t_t$) can be redefined by replacing $\Delta_n$ and $\Delta_t$ with $\Delta_{n,c}$ and $\Delta_{n,c}$ for both normal and tangential components(Eqn. 2.17) [66].

$$\begin{aligned} \Delta_{n,c} &= \Delta_n - \Delta_n^T \\ \Delta_{t,c} &= \Delta_t - \Delta_t^T \end{aligned} \tag{2.17}$$

Substituting the modified crack openings in Equation 2.17 to the Equation 2.7, gives

$$t_{n,c}\left(\Delta_{n,c},\Delta_{t,c}\right)=\frac{\mathrm{r}_n}{\delta_n}\left[\mathrm{k}\left(1-\frac{\Delta_{n,c}}{\delta_n}\right)^a\left(\frac{k}{a}+\frac{\Delta_{n,c}}{\delta_n}\right)^{k-1}-\mathrm{a}\left(1-\frac{\Delta_{n,c}}{\delta_n}\right)^{a-1}\left(\frac{k}{a}+\frac{\Delta_{n,c}}{\delta_n}\right)^k\right]\left[\mathrm{r}_t\left(1-\frac{|\Delta_{t,c}|}{\delta_t}\right)^b\left(\frac{k}{a}+\frac{|\Delta_{t,c}|}{\delta_n}\right)^l+G_{II}-G_I\right] \tag{2.18a}$$

$$t_{t,c}\left(\Delta_{n,c},\Delta_{t,c}\right)=\frac{\mathrm{r}_t}{\delta_t}\left[\mathrm{l}\left(1-\frac{|\Delta_{t,c}|}{\delta_t}\right)^b\left(\frac{l}{b}+\frac{|\Delta_{t,c}|}{\delta_t}\right)^{l-1}-\mathrm{b}\left(1-\frac{|\Delta_{t,c}|}{\delta_t}\right)^{b-1}\left(\frac{l}{b}+\frac{|\Delta_t|}{\delta_t}\right)^l\right]\left[\mathrm{r}_n\left(1-\frac{\Delta_{n,c}}{\delta_n}\right)^a\left(\frac{k}{a}+\frac{\Delta_{n,c}}{\delta_n}\right)^k+G_I-G_{II}\right]\frac{\Delta_{n,c}}{|\Delta_{t,c}|} \tag{2.18b}$$

The thermal considerations may include heat conduction between the surfaces due to fiber bridging and heat generation due to cracking, other than thermal expansion of the fiber and matrix in a composite material. The aforementioned extensions for potential-based cohesive zone model are proposed analytically and can be implemented computationally. Since the results to the above expansions require a thorough experimental work, it is beyond the scope of this study.

# 3. BEAMS AND PLATES UNDER THERMAL AND MECHANICAL LOADS

## 3.1 A Bi-Material Plate under Thermal and Mechanical Loading with Energy Methods

A beam under thermal and mechanical loads is studied with three beam theories, i.e. Euler-Bernoulli beam theory, Timoshenko beam theory and Reddy-Bickford third order beam theory. The governing equilibrium equations (Euler equations) can be derived using the principle of minimum potential energy for each plate theory. The equations are given in terms of the internal stress resultants. The constitutive equations of linear elasticity are utilized to relate the stress resultants of each theory to the components of the strain. These relationships are then utilized express the equations of motions in terms of the displacement field variables.

### *3.1.1 Euler-Bernoulli Beam Theory*

The simplest beam theory is the Euler-Bernoulli Beam theory. It is based on a displacement field given as

$$U(x,z) = u(x) - z\left[\frac{dw}{dx}\right] \tag{3.1}$$

$$W(x,z) = w(x) \tag{3.2}$$

where U and W are the displacements in x- and z-directions, respectively. The displacement field given above dictates for the straight lines normal to the mid-plane of the beam before deformation the following; They remain straight and normal to the mid-plane after deformation.Hence, both transverse shear and transverse normal strains are neglected. From the above displacement field, the nonzero linear strains

can be calculated as:

$$\begin{aligned} \varepsilon_x &= \varepsilon^0 + z\varepsilon^1 \\ \varepsilon^0 &= \frac{du}{dx} \\ \varepsilon^1 &= -\frac{d^2w}{dx^2} \end{aligned} \tag{3.3}$$

The stress-strain relations in a laminate for the $k_{th}$ lamina in the thickness direction are

$$\sigma_x^k = E^k \left(\varepsilon_x - \alpha^k \Delta T\right) \tag{3.4}$$

Where $E^k$ is the elastic modulus, $\alpha^k$ is the thermal expansion coefficient of the $k^{th}$ lamina, and $\Delta T$ is the temperature rise in the beam. Considering the following for the stress resultants

$$(N, M) = \sum_{i=1}^{k} \int_{z^k}^{z^{k+1}} \sigma_x^k \left(1, z^2\right) dA \tag{3.5}$$

The relation between these resultants and the strains are

$$\left\{ \begin{array}{c} N \\ M \end{array} \right\} = \left[ \begin{array}{cc} A_{11} & B_{11} \\ B_{11} & D_{11} \end{array} \right] \left\{ \begin{array}{c} \varepsilon^0 \\ \varepsilon^1 \end{array} \right\} - \left\{ \begin{array}{c} N^T \\ M^T \end{array} \right\} where \tag{3.6}$$

$$(A_{11}, B_{11}, D_{11},) = \sum_{i=1}^{k} \int_{z^k}^{z^{k+1}} E^k \left(1, z, z^2,\right) dA \tag{3.7}$$

$$\left(N^T, M^T\right) = \sum_{i=1}^{k} \int_{z^k}^{z^{k+1}} E^k \alpha^k \Delta T dA \tag{3.8}$$

The governing equations and the boundary conditions for a displacement field and constitutive equations can be obtained using the minimum potential energy (MTPE),

$$\begin{aligned} \frac{dN}{dx} &= 0 \\ \frac{d^2M}{dx^2} &= 0 \end{aligned} \tag{3.9}$$

### *3.1.2 Timoshenko Beam Theory*

Timoshenko beam theory is based on a displacement field

$$U(x,z) = u(x) + z\varphi W(x,z) = w(x) \tag{3.10}$$

Where $\varphi$ is the rotation of the neutral axis of the beam. In the Timoshenko beam theory, different than the Euler beam theory, the straight lines normal to the mid-plane of the beam before deformation does not remain straight after the deformation, since the rotation is independent of the slope of the neutral axis and transverse shear strain across the thickness is constant (thus constant shear stress). The Timoshenko beam theory requires shear correction factors due to this constant shear stress assumption. The above displacement field gives the following strains

$$\begin{aligned} \varepsilon_x &= \varepsilon^0 + z\varepsilon^1 \\ \gamma_{xz} &= \gamma^0 \\ \varepsilon^0 &= \frac{du}{dx} \\ \varepsilon^1 &= \frac{d\varphi}{dx} \\ \gamma^0 &= \varphi + \frac{dw}{dx} \end{aligned} \tag{3.11}$$

In addition to the normal and moment stress resultants we have a shear resultant Q

$$\{Q\} = [A_{55}]\left\{\gamma^0\right\} \tag{3.12}$$

where

$$A_{55} = \sum_{i=1}^{k} \int_{z^k}^{z^{k+1}} G^k dA \tag{3.13}$$

Using MTPE, the governing equations and corresponding boundary conditions for

the displacement field and constitutive equations are derived as

$$\begin{aligned} \frac{dN}{dx} &= 0 \\ \frac{d^2M}{dx^2} - Q &= 0 \\ \frac{dQ}{dx} &= 0 \end{aligned} \tag{3.14}$$

### *3.1.3 Reddy-Bickford Third Order Beam Theory*

In this third order beam theory, the displacement field is given as

$$\begin{aligned} U(x,z) &= u(x) + z\varphi - \frac{4}{3h^2}z^3\left(Q(x) + \frac{dw}{dx}\right) \\ W(x,z) &= w(x) \end{aligned} \tag{3.15}$$

The above displacement field gives the following strains

$$\begin{aligned} \varepsilon_x &= \varepsilon^0 + z\varepsilon^1 + z^3\varepsilon^3 \\ \gamma_{xz} &= \gamma^0 + z^2\gamma^2 \\ \varepsilon^0 &= \frac{du}{dx} \\ \varepsilon^1 &= \frac{d\varphi}{dx} \\ \varepsilon^3 &= -\frac{4}{3h^2}\left(\frac{d\varphi}{dx} + \frac{d^2w}{dx^2}\right) \\ \gamma^0 &= \varphi + \frac{dw}{dx} \\ \gamma^2 &= -\frac{4}{h^2}\left(\varphi + \frac{dw}{dx}\right) \end{aligned} \tag{3.16}$$

Considering the following for the stress resultants

$$(N, M, P) = \int_A \sigma_x^k \left(1, z^2, z^3\right) dA \tag{3.17}$$

The relation between these resultants and the strains are

$$\left\{ \begin{array}{c} N \\ M \\ P \end{array} \right\} = \left[ \begin{array}{ccc} A_{11} & B_{11} & E_{11} \\ B_{11} & D_{11} & F_{11} \\ E_{11} & F_{11} & H_{11} \end{array} \right] \left\{ \begin{array}{c} \varepsilon^0 \\ \varepsilon^1 \\ \varepsilon^3 \end{array} \right\} - \left\{ \begin{array}{c} N^T \\ M^T \\ P^T \end{array} \right\} \tag{3.18}$$

where

$$(A_{11}, B_{11}, D_{11}, E_{11}, F_{11}, H_{11}) = \sum_{i=1}^{k} \int_{z^k}^{z^{k+1}} E^k \left(1, z, z^2, z^3, z^4, z^6\right) dA \tag{3.19}$$

$$\left(N^T, M^T, P^T\right) = \sum_{i=1}^{k} \int_{z^k}^{z^{k+1}} E^k \alpha^k \Delta T \left(1, z, z^3\right) dA \tag{3.20}$$

Again, minimum total potential energy provides the governing equations and associated boundary conditions as

$$\begin{aligned} \frac{dN}{dx} &= 0 \\ \frac{dM}{dx} - \frac{4}{3h^2}\frac{dP}{dx} - Q + \frac{4}{h^2}S &= 0 \\ \frac{dQ}{dx} - \frac{4}{h^2}\frac{dS}{dx} + \frac{4}{3h^2}\frac{d^2P}{dx^2} &= 0 \end{aligned} \tag{3.21}$$

### *3.1.4 Comparison of the Results*

A bi-material beam with two layers assumed to be clamped at left end and free at the right end. There is a uniform temperature change of 100 C. In the second case, in addition to the thermal load, a transverse load of 1 N is applied at the left end of the beam (Fig. 3.1). The beam is 100 mm long the two layers are of the same thickness. The thickness of one layer is equal to 10 mm for thick beam case and 2.5 mm for thin beam case, which give a slenderness ratio of 1/5 and 1/20. The material properties used for Material 1 and Material 2 is given in Table 3.1.

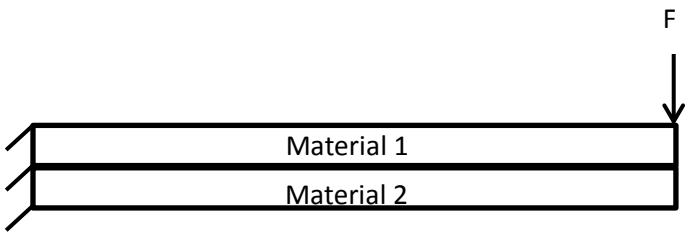


Figure 3.1: Bi-material beam under thermal and mechanical loads

Table 3.1: Material properties

| | Material 1 | Material 2 |
|---|---|---|
| Elastic Modulus[MPa] | 343000 | 105000 |
| Shear modulus [MPa] | 144117 | 38321 |
| Poissons ratio | 0.19 | 0.37 |
| Coeff. of thermal expansion [1/C] | 8.6e-6 | 9.1e-6 |

It is seen that without mechanical load, applying only thermal load gives the same results for u and w in Euler-Bernoulli and Timoshenko beam theories. The results obtained by Euler- Bernoulli and Timoshenko for a thick beam are compared in Figure 3.2.

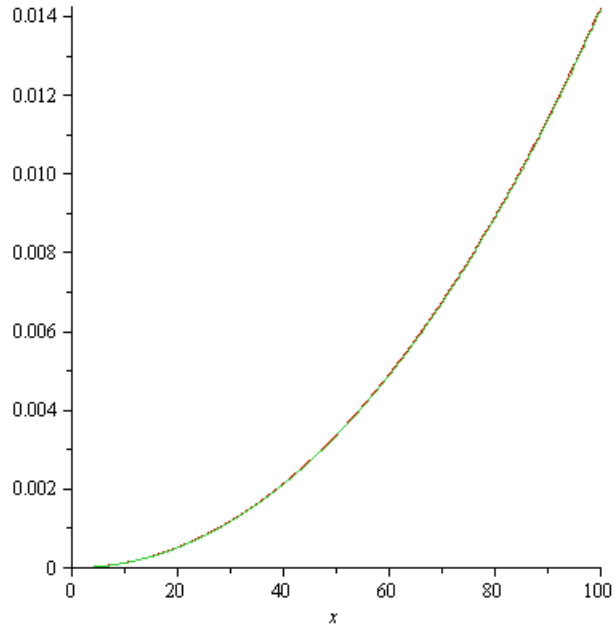


Figure 3.2: Euler-Bernoulli and Timoshenko deflection comparison in a thick beam

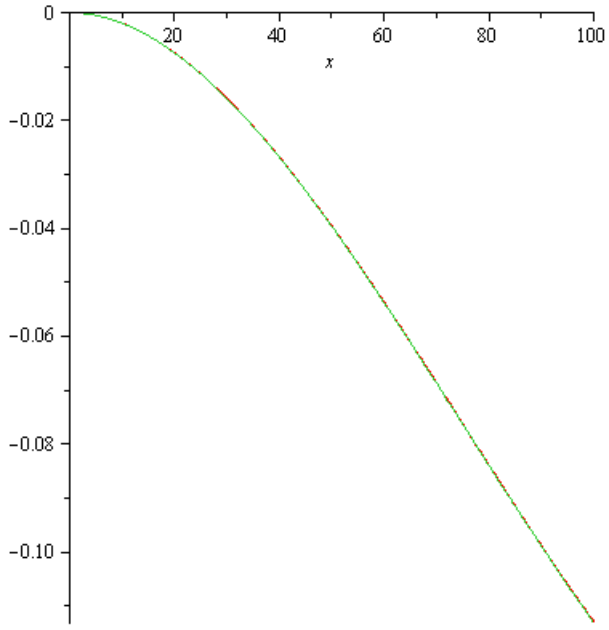


Figure 3.3: Euler-Bernoulli and Timoshenko deflection comparison in a thin beam

As it can be seen from the graphs in Figure 3.2 for the thick beam the thermal residual stresses are dominant and the beam curves upwards whereas for a thin beam the deflection due to transverse load is higher (Fig. 3.3) and the curve concaves down. There is a minor difference between the solutions of deflections by Euler-Bernoulli and Timoshenko beam theories. When we compare the Euler-Bernoulli for thin and thick beam we get the following results.

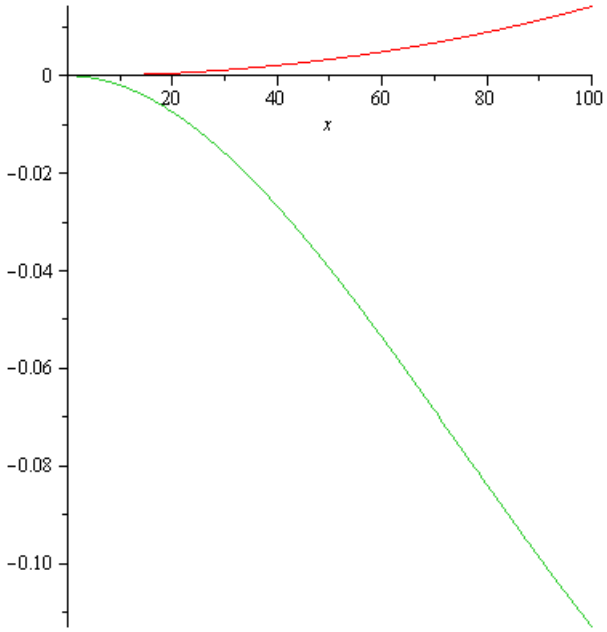


Figure 3.4: Timoshenko beam deflection for a thin and a thick beam under thermal and mechanical load

And when the Timoshenko beam theory is used for thin and thick beam the results are as shown in Figures 3.4 and 3.5.

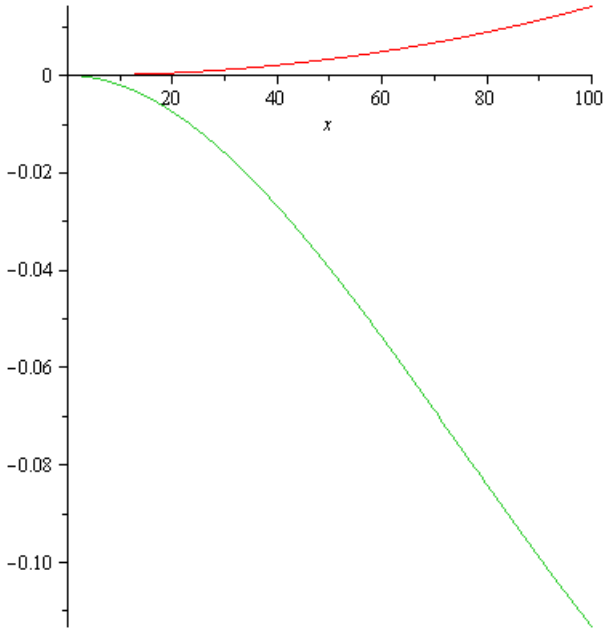


Figure 3.5: Timoshenko beam deflection for a thin and a thick beam under thermal and mechanical load

The Euler-Bernoulli and Timoshenko beam theories are used to solve a cantilever bi-material beam made of two layers of the same thickness. The results show that the deflection due to thermal load dominates the deflection due to the mechanical load when the beam is thick. The solutions for Euler-Bernoulli and Timoshenko have a minor difference in w(x) values at the free end of the beam.

## 3.2 Titanium Graphite (TiGr) Composite Plate under Thermal Load

Titanium-Graphite composites (TiGr) is a type of composite made of both polymer matrix composite and titanium sheets. It is developed to be used in aircrafts for high temperature applications. This study is done to benchmark the papers of Burianek and Spearing [67, 68], in which they investigated $[Ti/0/90/02]_s$ as the base laminate for the models to calculate the residual stresses developed when the laminate is cooled from 260°C to 177°C and further to 25°C. The difference between the coefficients of thermal for PMC and Ti causes that residual stresses develop in the laminate.The reason why they used a two step cooling is to see that thermally induced residual stresses creates a small difference between the crack growth rate at 177°C and 25°C [67, 68].

The bridged crack modeling is used to predict the propagation of a crack at the interface between the composite layers. Thermal residual stresses are ignored when calculating the stresses and strain energy release rate. The effect of thermal residual stresses cancel out when calculating $\Delta G$ and $K_{eff}$ (stress intensity factor) and their main effect is on R-ratio (ratio between $\sigma_{min}$ and $\sigma_{max}$) [67, 68]. However, in this study it there is no crack involved in the model. The same array of plies is created in order to see the displacements, strains and stresses developed in the laminate.

The titanium layers are of two different types, i.e. the titanium alloy and Ti-15-3, whereas the PMC composed of epoxy matrix with IM7 graphite fibers. The comparison of the properties are given in Table 3.2.

Table 3.2: The material properties used in TiGr model

| | Epoxy | Ti | Ti-15-3 | IM7 |
|---|---|---|---|---|
| $E_1$ $[Pa]$ | 134000 | 106000 | 107000 | 155000 |
| $E_2$ $[Pa]$ | 9500 | 106000 | 112000 | 69000 |
| $E_3$ $[Pa]$ | 9500 | | | |
| $\nu_1 2$ | 0.3 | 0.36 | 0.33 | 0.35 |
| $\nu_2 3$ | 0.3 | | | |
| $\nu_1 3$ | 045 | | | |
| $G_{12}$ $[Pa]$ | 4900 | | 41400 | 5100 |
| $G_{13}$ $[Pa]$ | 4900 | | | |
| $G_{23}$ $[Pa]$ | 4900 | | | |
| $\alpha_{11}$ | 9E-07 | 8.6E-06 | 8.6E-06 | 9E-07 |
| $\alpha_{22}$ | 4.5E-06 | | | 4.5E-06 |
| $\alpha_{22}$ | 4.5E-06 | | | 4.5E-06 |

A $[Ti/0/90/0_2]_s$ layup of a $76 \times 19$ mm rectangular and a $76 \times 76$ square composite plate were modelled in 3D to see the thermal residual stresses developed in the part. Only one quarter of this specimen $(76 \times 19)$ mm is modelled and symmetry boundary conditions are used as shown in Figure 3.6. The square plate is developed to see if there is an effect of the geometry on the distribution of stresses at the free edges.

3D-stress element with eight nodes was used. The number of elements are 76 and 19 in $76 \times 19$ mm plate and 76 and 76 in $76 \times 76$ mm plate along the directions 1 and 2. There are only one row of elements in each layer. The thicknesses of titanium sheet and composite lamina are 0.127 mm and 0.142 mm, respectively.

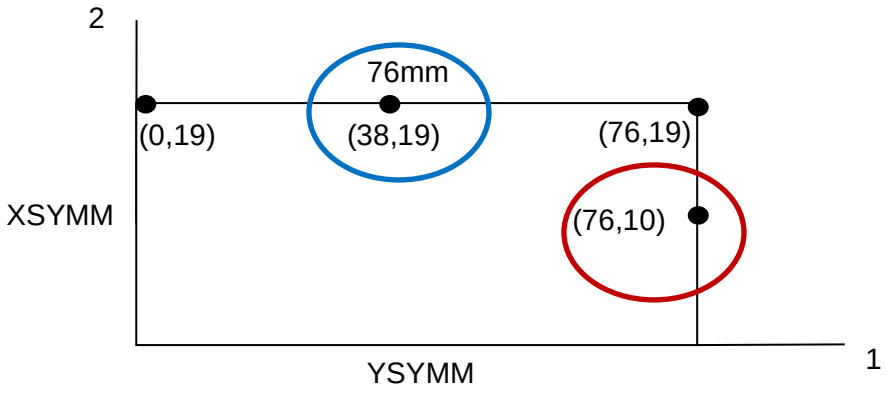


Figure 3.6: The schematic of the model. The circles indicate the points at which the results are given

The thermal expansion coefficient (CTE) of the titanium alloy is $8.6 \times 10 - 6°C$, and CTE of the composite lamina is $0.9 \times 10 - 6°C$ in the longitudinal (fiber) direction and $4.5 \times 10 - 6°C$ in the transverse direction.

TiGr composite is assumed to be stress-free at 260°C [67]. In the model, the plate is initially at 260°C then cooled to 177°C first and further to 25°C.

### *3.2.1 Results*

The rectangular and square plates did not show almost any differences in the stress distribution and for this reason only the results for the rectangular plate with the base laminate configuration is represented in this paper. When the part is cooled, it bulged out in the middle section, which consist of the 0-degree plies (Fig. 3.7). All the results are taken at the middle points (38,19) and (76,10) of the free edges are the results at the integration points.

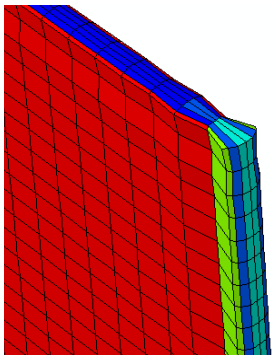

Figure 3.7: The stress contour plot is taken for a rectangular $[Ti/0_2]_s$ laminate

As it is seen in the Figure 3.8, the displacement along the fibers is constant on the surface which has normal in 2- direction (surface-2), whereas is continuous and slightly increasing towards the middle of the thickness of the plate where the plies are unidirectional. In Figure 3.9, the surface having normal in 1-direction ( surface-1) has constant displacement and there is a continuous increase towards the middle unidirectional plies on surface-2.

The strain distribution through the thickness can be seen in Figures 3.10 and 3.11. All the plies are in compression but the values differ in titanium sheet, transverse and unidirectional plies. The unidirectional plies are more contracted in the transverse

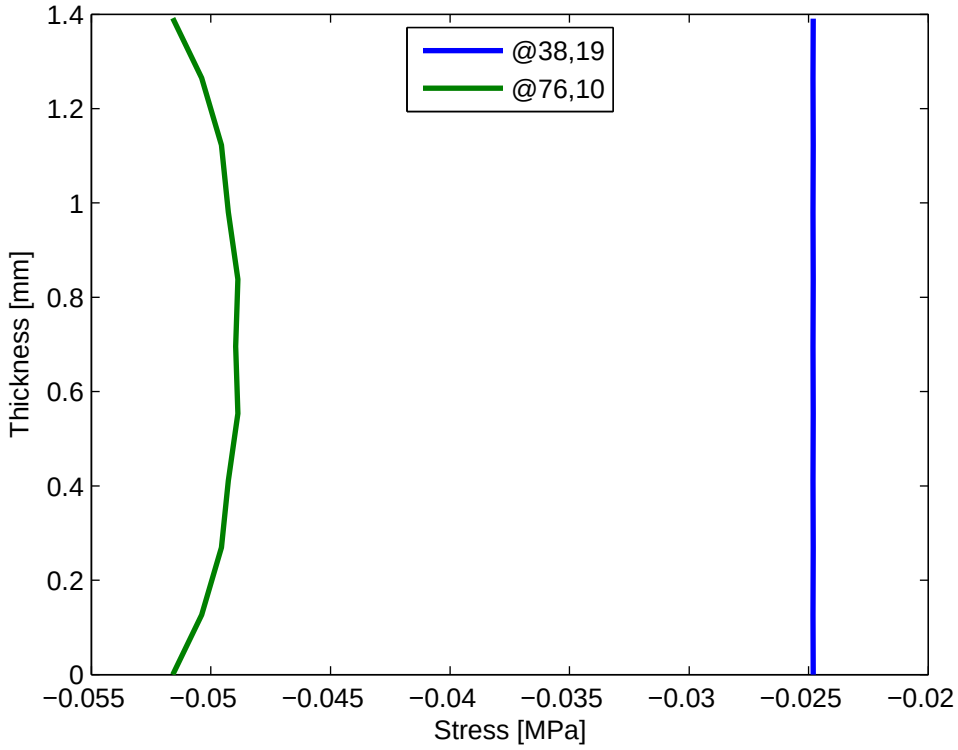


Figure 3.8: Displacements in longitudinal direction ($U_1$) through the thickness at middle points of the free edges

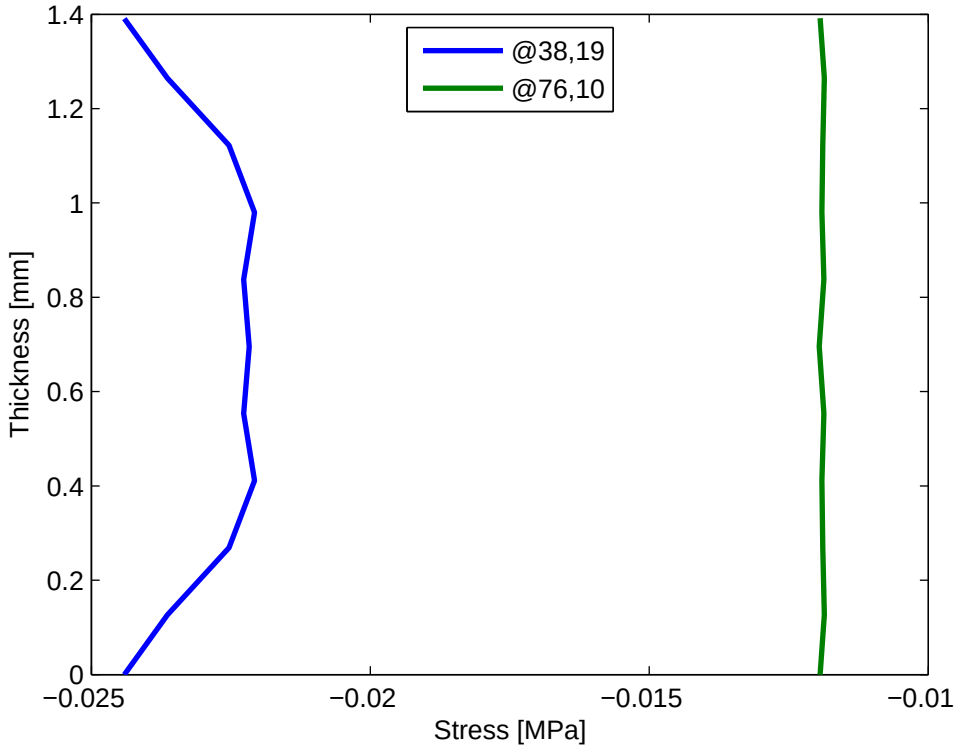


Figure 3.9: Displacements in transverse direction ($U_2$) through the thickness at middle points of the free edges

direction and titanium is in the highest compression since it has the highest coefficient of thermal expansion.

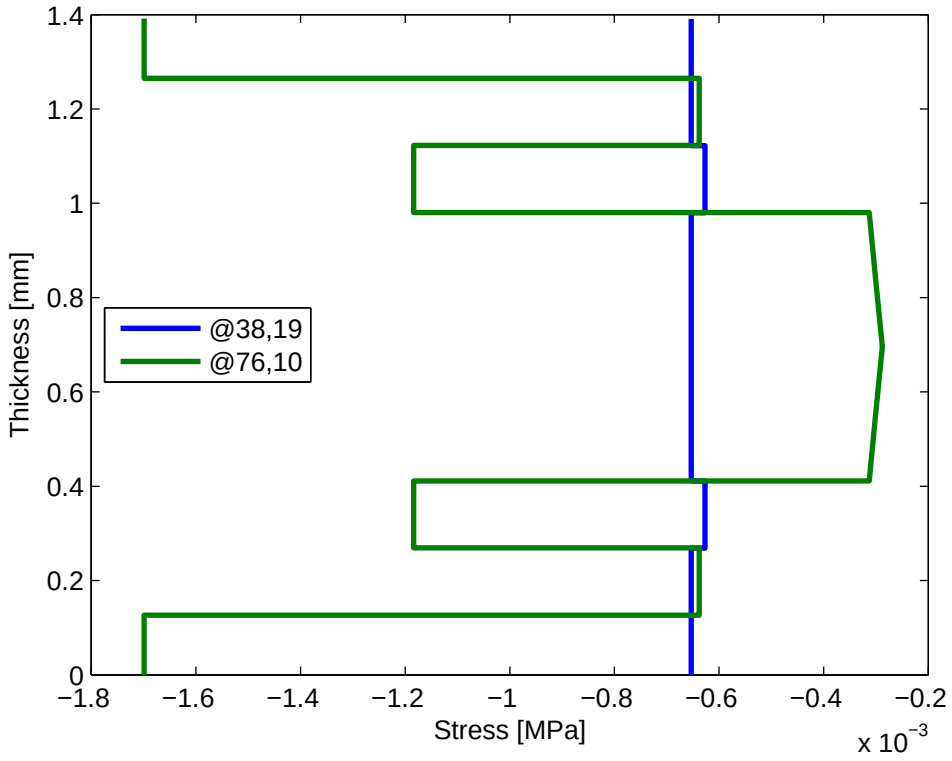


Figure 3.10: Strain distributions in longitudinal direction through the thickness at middle points of the free edges

The stresses are shown in Figures 3.12, 3.13 and 3.14. Only the top and bottom titanium plies are in tensional normal stress of 163 MPa and the rest is in compression where lowest is almost 60 MPa in the 90-degree plies. The normal stress $S_{22}$ is tensional throughout the thickness except in second and ninth plies which are the 0-degree plies in contact with the titanium layer.

In the paper of Burianek and Spearing [67] it is reported that the thermal residual

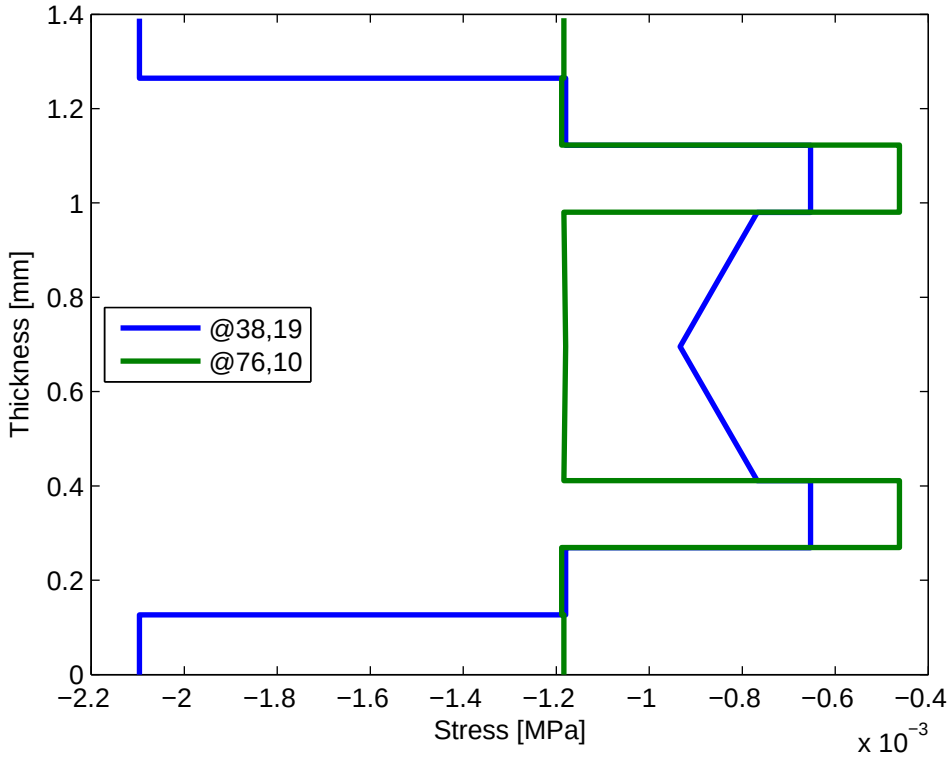


Figure 3.11: Strain distributions in transverse direction through the thickness at middle points of the free edges

stress in the titanium ply of the laminate ($[Ti/0/90/02]_s$), is approximately 159 MPa. The results are in agreement with the aforementioned work and the small difference may be arisen due to the slight differences in the material properties used in the two models.

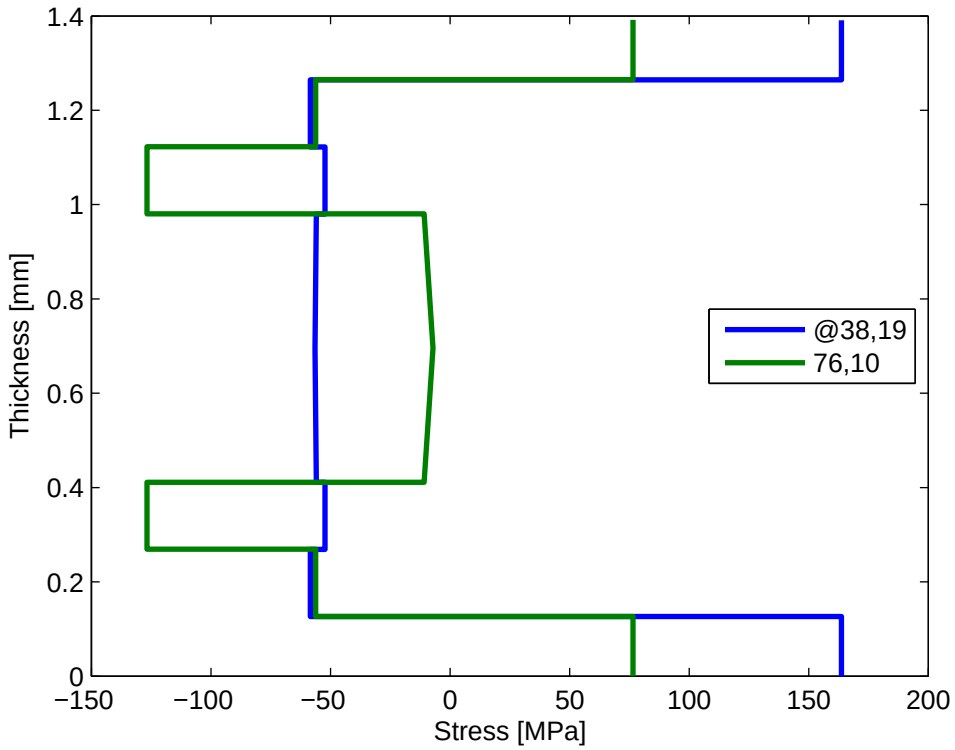


Figure 3.12: Normal stress distribution in 1-direction through the thickness at the middle points of the free edges

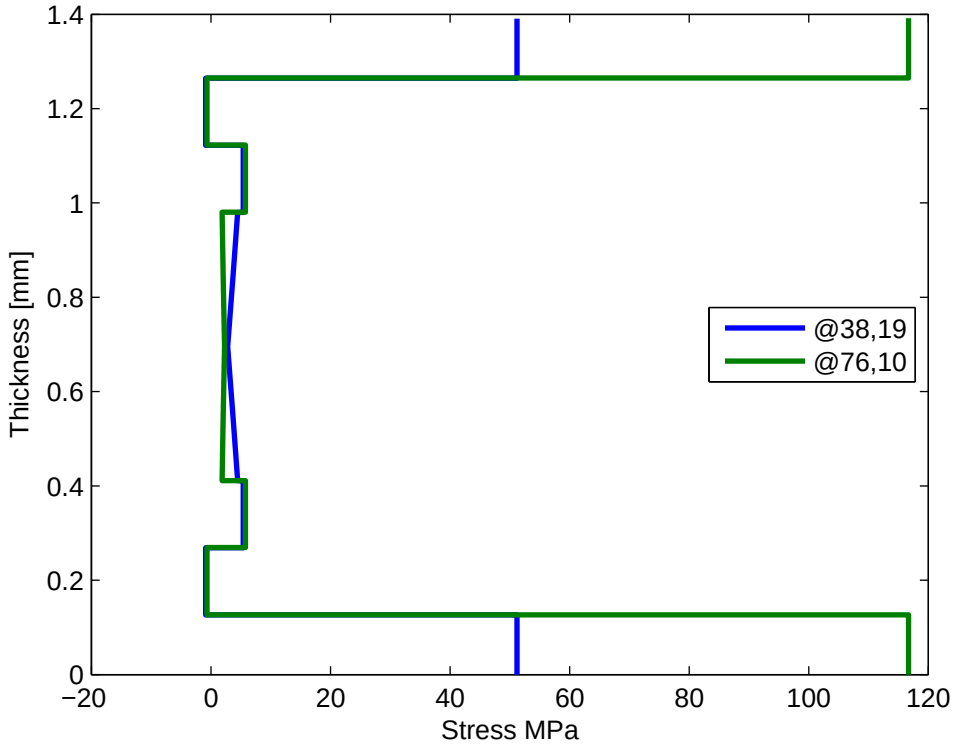


Figure 3.13: Normal stress distribution in 2-direction through the thickness at the middle points of the free edges

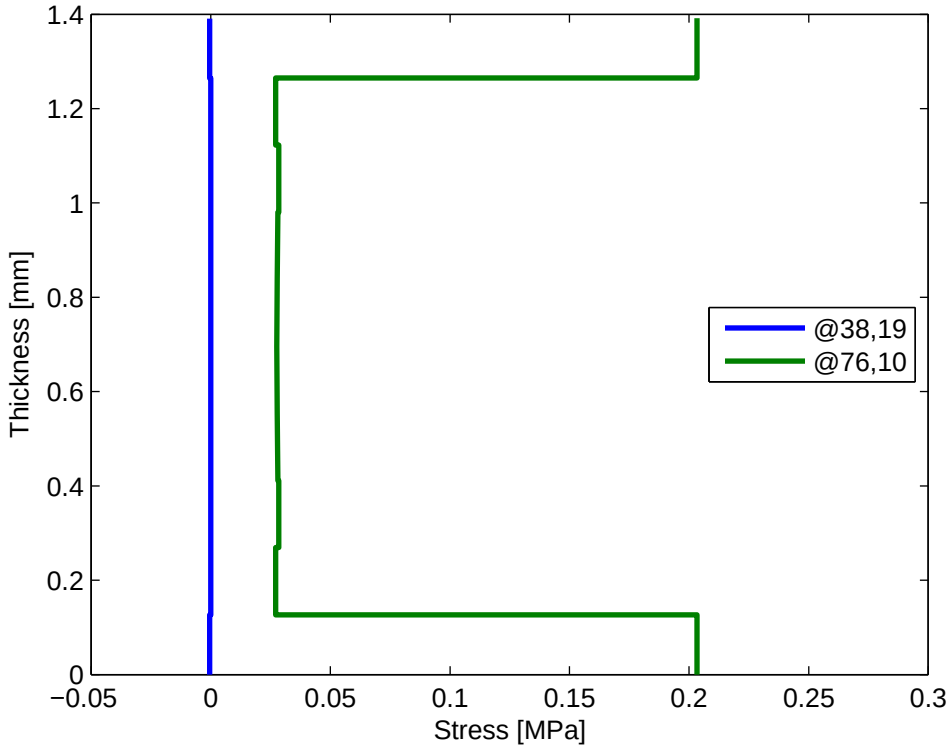


Figure 3.14: Shear stress distribution through the thickness at the middle points of the free edges

# 4. PARAMETRIC STUDY OF ADHESIVE JOINT MODELS UNDER MECHANICAL AND THERMAL LOADING USING A COHESIVE ZONE MODEL

One of the tasks necessary for the engineer to perform in the design of structures is failure analysis. A structural failure analysis is the process of evaluating the deformations and stress distributions of a structure to insure the element can perform under the prescribed operating conditions. This is often accomplished through the aid of finite element software, as most structures and loadings do not permit exact solutions of the elasticity equations. Since interfaces are the most critical regions in structures, interfacial fracture and debonding in adhesive joints under mechanical and thermal loading has been investigated in numerous papers.

In heterogeneous materials (i.e. PMCs), thermal residual stresses are generated during composite processing by both chemically induced shrinkage and/or CTE mismatch. The large thermal strain introduced during the curing cycle can cause fiber/matrix debonding in the composites. The material datasheet obtained from the manufacturer ,for an epoxy which exhibits high-shrinkage, shows that considering that the epoxy shrinks about 0.6% is acceptable. In order to mirror the chemical shrinkage in the model, one can add a fictitious step in the analysis, at which temperature drops, so that the matrix shrinks as if it is due to curing process.quivalent thermal contraction is applied on the matrix, based on the thermal expansion coefficient of epoxy. A temperature drop of 120°C provides the desired value of shrinkage for the epoxy used.

Structural adhesives are commonly used to connect similar or dissimilar materials in many industries such as aerospace and automotive, since they are advantageous

for being light weight and not causing stress concentrations as bolts and rivets do. Those structures operating in hostile environments can generate thermal stresses which need to be taken into account. Results showed that joint performance varies with temperature.

## 4.1 Double Cantilever Beam Model

A double cantilever beam test serves to obtain Mode I interlaminar fracture toughness, so called the critical strain energy release rate (ASTM Standard D 5528-01). Energy solutions for a bimaterial double cantilever beam provides the strain energies in the top and bottom parts of the double cantilever beam is given as,

$$U_1 = \frac{1}{2}\int_0^h \frac{M_a^2}{E_a I_a}$$
$$U_2 = \frac{1}{2}\int_0^h \frac{M_b^2}{E_b I_b} \tag{4.1}$$

This study incorporates the adhesive interface, which is assumed elastic, and failure analysis of PMC/PMC and PMC/metal interfaces in double cantilever beams. First, two different models are created to account for two different type of interfaces in finite element analysis. The FE analysis is employed geometric nonlinearity, and coefficient of thermal expansion. Two finite element models is proposed to analyze failure for two different interfaces subjected to a mode-I fracture. In a cohesive zone method, the constitutive response of the cohesive element can be determined by the traction-separation law. Potential based cohesive zone model with a polynomial traction-separation constitutive behavior is used to model the interface properties.

### *4.1.1 Material Properties and Testing*

The hybrid composite laminates are composed of either T650 8-harness woven fabric with or without CNTs and having no titanium foil in its layup with epoxy matrix (EPON 862) or T300 plain weave carbon fabric with CNTs (fuzzy fabric), plain Titanium foil, Titanium foil with CNTs (fuzzy Ti-foil), and epoxy matrix (EPON 862)(Fig. 4.1). Carbon nanotubes are grown on both faces of a T300 fabric using the carbon vapor deposition method. Similarly, fuzzy Ti-foil has CNTs grown on one of its faces. The pre-crack, created by Teflon film, is located between the Titanium foil and and the fuzzy fabric interface. During curing process temperature goes up to 177°C, which induced a 0.6% cure shrinkage. The chemical shrinkage is considered in numerical analysis for both type of specimens (i.e. with Ti-foil and without Ti-foil).

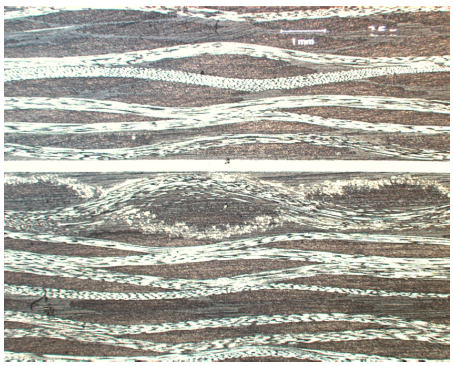

Figure 4.1: SEM image of the Ti-foil layer between two PMC layers (courtesy of Dr. Ochoa's group)

The effective material properties for T650 8-harness woven fabric with epoxy matrix (EPON 862), and T300 plain weave carbon fabric with epoxy matrix (EPON

862) are calculated using micromechanics. Table 4.1 shows the required engineering constants, i.e. elastic modulus, Poisson's ratio and shear modulus, in normal and shear directions. The fiber-volume fraction is assumed to be 66.3% (Table 4.2).

Table 4.1: Engineering constants for T650 8-harness woven fabric, and T300 plain weave carbon fabric with EPON 862

| | | |
|---|---|---|
| $E_1$ $[Pa]$ | 7.36E+10 | 5.67E+10 |
| $E_2$ $[Pa]$ | 7.36E+10 | 5.67E+10 |
| $E_3$ $[Pa]$ | 9.03E+09 | 7.78E+09 |
| $\nu_1 2$ | 0.027841 | 0.0690 |
| $\nu_2 3$ | 0.511445 | 0.4134 |
| $\nu_1 3$ | 0.511445 | 0.4134 |
| $G_{12}$ $[Pa]$ | 4.84E+09 | 2.54E+09 |
| $G_{23}$ $[Pa]$ | 3.77E+09 | 2.09E+09 |
| $G_{13}$ $[Pa]$ | 3.77E+09 | 2.09E+09 |

Table 4.2: Fiber volume fractions in matrix for T650 8-harness woven fabric, and T300 plain weave carbon fabric with EPON 862

| | T650 | T300 |
|---|---|---|
| $V_{\text{fiber in matrix}}$ | 66.3% | 57.15% |

High temperature double cantilever beam test was performed in an oven at 110 C. The oven was heated up to the testing temperature before the specimen was loaded to the test frame.(Figures 4.2, 4.3).

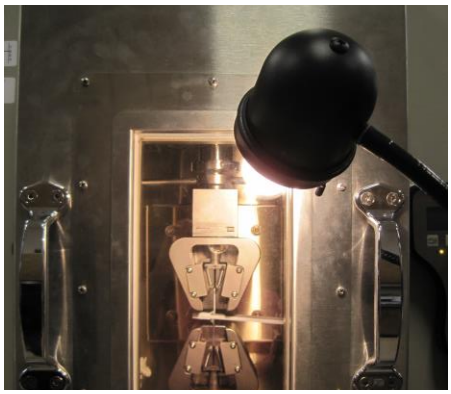

Figure 4.2: DCB test setup (courtesy of Dr. Ochoa's group)

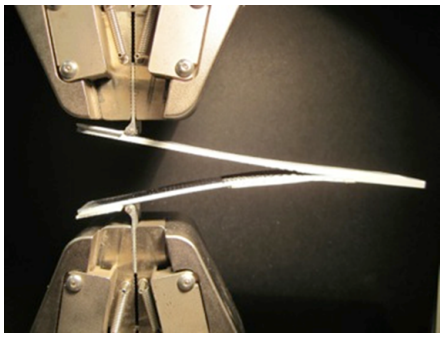

Figure 4.3: DCB test setup. Specimen placed between grips of the tensile test machine (courtesy of Dr. Ochoa's group)

Two sketches of double cantilever beam models with and without a Ti-Foil (Figures 4.4, 4.5) has been given to explain the layup of the DCB specimen, and a work has been conducted to observe the effect of various process parameters and interface properties.


Figure 4.4: DCB specimen sketch representing specimens without titanium foil

In the first model (Fig. 4.4), the top and bottom arms of the double cantilever beam consists of polymer-matrix composite layers, which are made of T650 fuzzy and non-fuzzy fabrics. Red line is the interface where cohesive elements are placed.


Figure 4.5: DCB specimen sketch representing specimens with a titanium foil

In the second model (Fig. 4.5), PMC layers are made of T300 fuzzy and non-fuzzy fabrics with titanium-foil. Here, the Ti- foil is shown thicker than its actual thickness to ease the visibility for the reader. Also, both of the sketches do not represent actual ratios of their width and height.

### *4.1.2 Finite Element Solution - Prediction of Interface Properties*

For a better understanding and control of the cohesive zone properties, interface strength, fracture energy, initial slope indicators has been studied parametrically. Also, a mesh study is conducted to see the effect of the cohesive element size. The double cantilever beam is considered 160 mm long and 20 mm wide, whereas the thickness of one arm is 1.98 mm.

The analysis is static and controlled by displacement, which is applied to open the arms at the end with a pre-crack (Fig. 4.6). Plain strain elements are used for each half of the beam.

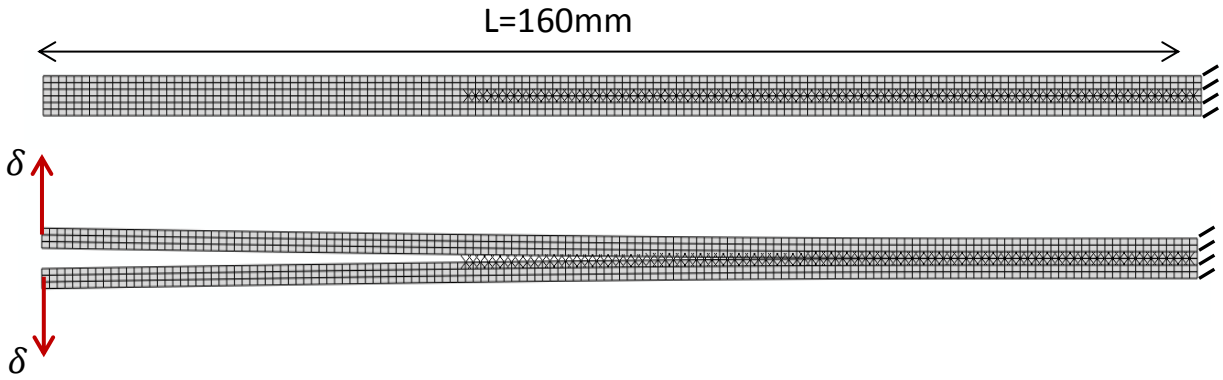


Figure 4.6: Geometry and loading conditions in DCB model

Cohesive elements are placed between two arms of the DCB specimen and they share the top and bottom row of nodes on the top and bottom arms, respectively, hence they have zero-thickness based on the geometric coordinates of their nodes. In order to show the effect of the mesh refinement and cohesive element size, the arms of DCB specimen without the titanium foil is modeled with 3, 4, and 7 rows of four node plane strain elements (CPE4), in three different mesh refinements, in which the cohesive element the plane strain element (CPE4) length varies as 1 mm, 0.5 mm and 0.25 mm, respectively (Figures 4.7-4.9).

In Ti-foil specimen model, the titanium layer is represented by a single row of elements, whereas the upper and lower PMC layers have 8 elements through the thickness direction. Ti-foil is assumed to be perfectly bonded to the PMC layer at its upper surface, whereas, cohesive interface elements are embedded at the lower interface. Since titanium and PMC has different CTEs, thermal strains are taken

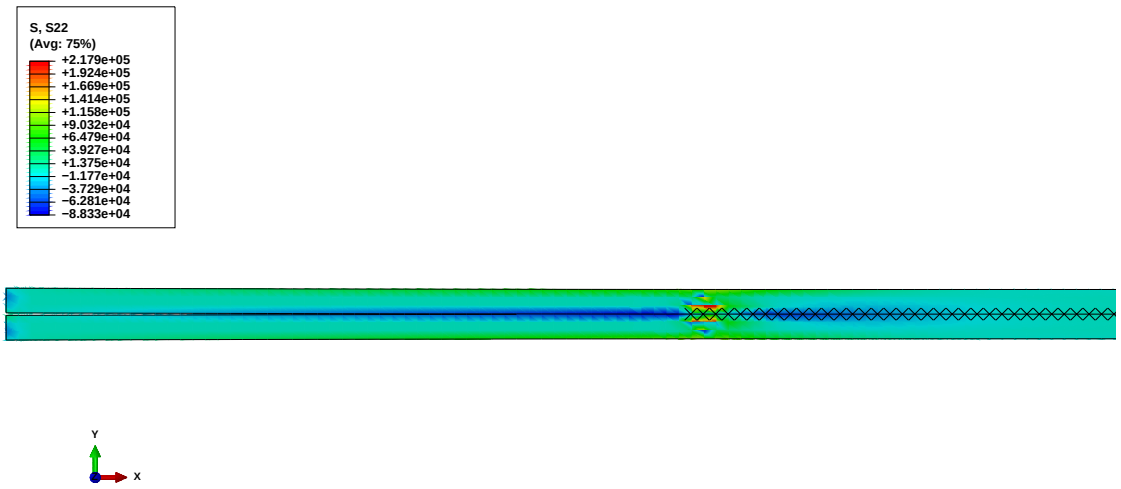


Figure 4.7: DCB stress distribution with 1 mm length element

into account.

In the Figures 4.7, 4.8, and 4.9, normal stress contour plots are given. Here, it can be seen that the mesh size is quite effective in stress distributions at crack tip. Cohesive zone parameters should be recalculated for different cohesive element lengths to obtain the same behavior at the interface (Fig. 4.10).

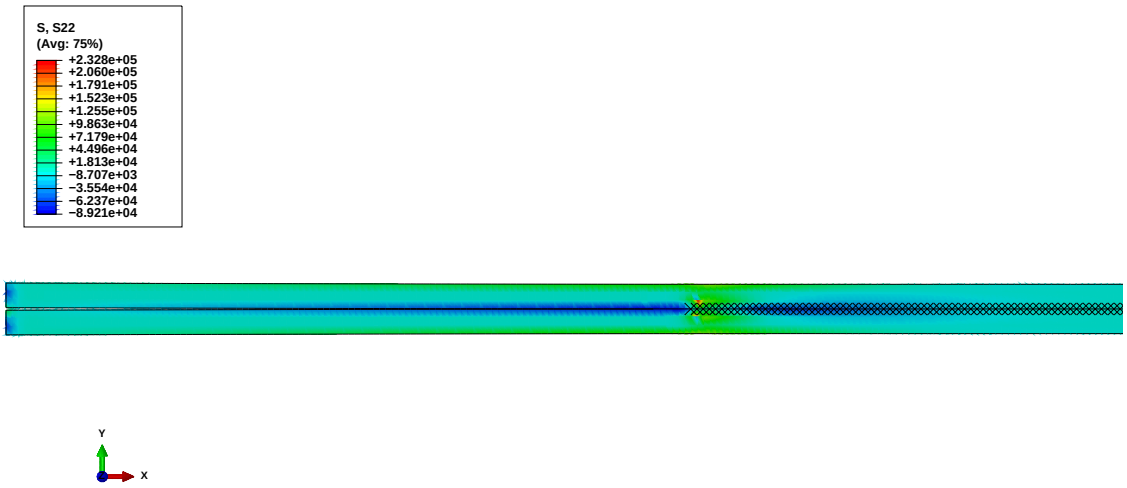


Figure 4.8: DCB stress distribution with 0.5 mm length element

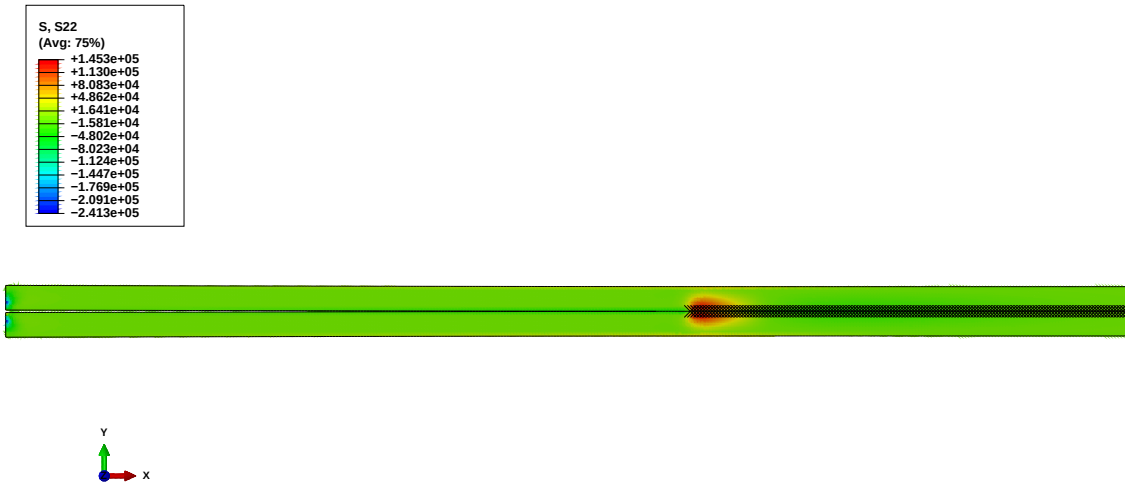


Figure 4.9: DCB stress distribution with 0.25 mm length element

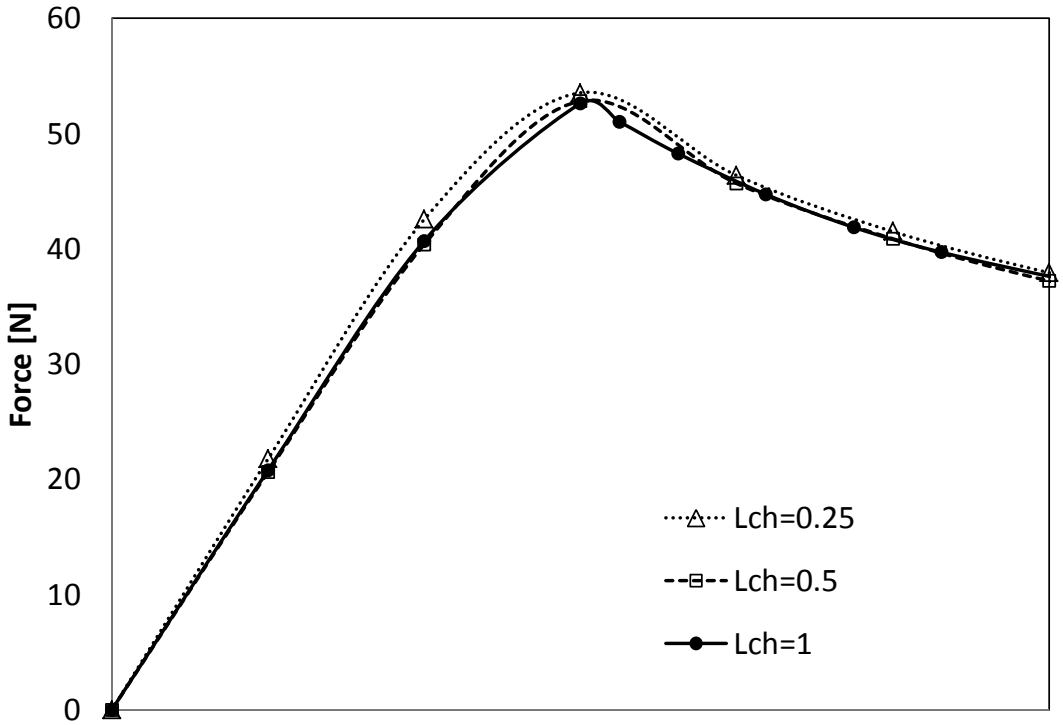


Figure 4.10: Comparison of the overall force-displacement response with different cohesive element length

Force vs. displacement curve is investigated for different interface strengths keeping the fracture energy constant. In that case, the force required to initiate the propagation of the crack decreases with decreasing interface strength as expected (Fig. 4.11).

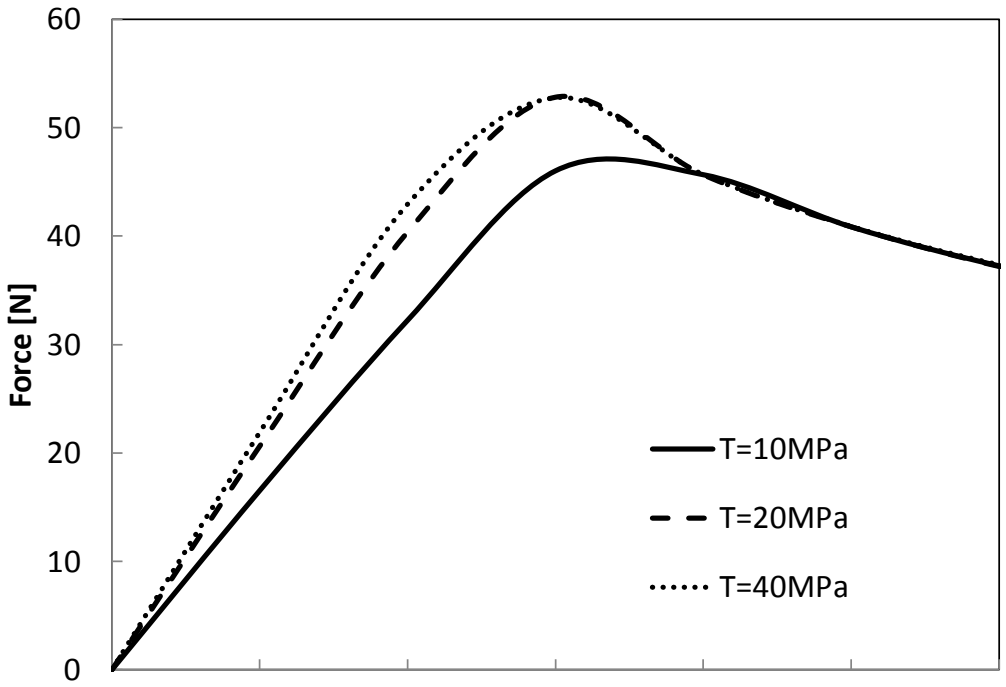


Figure 4.11: Effect of changing the interface strength on the global force-displacement behavior

Interface strength (T) in the aforementioned double cantilever beam (DCB) (with and without Ti-Foil layer,namely non-Ti,with-Ti) at room temperature is investigated. Fracture toughness ($G_I$) is obtained from the DCB tests. In Figure 4.12, $G_I$ vs. delamination length is extracted from the test data for fuzzy and nun-fuzzy non-Ti specimens. Experimentally, it is found that $G_I$ values for specimen with CNTs are almost twice as higher than the interface without CNTs.

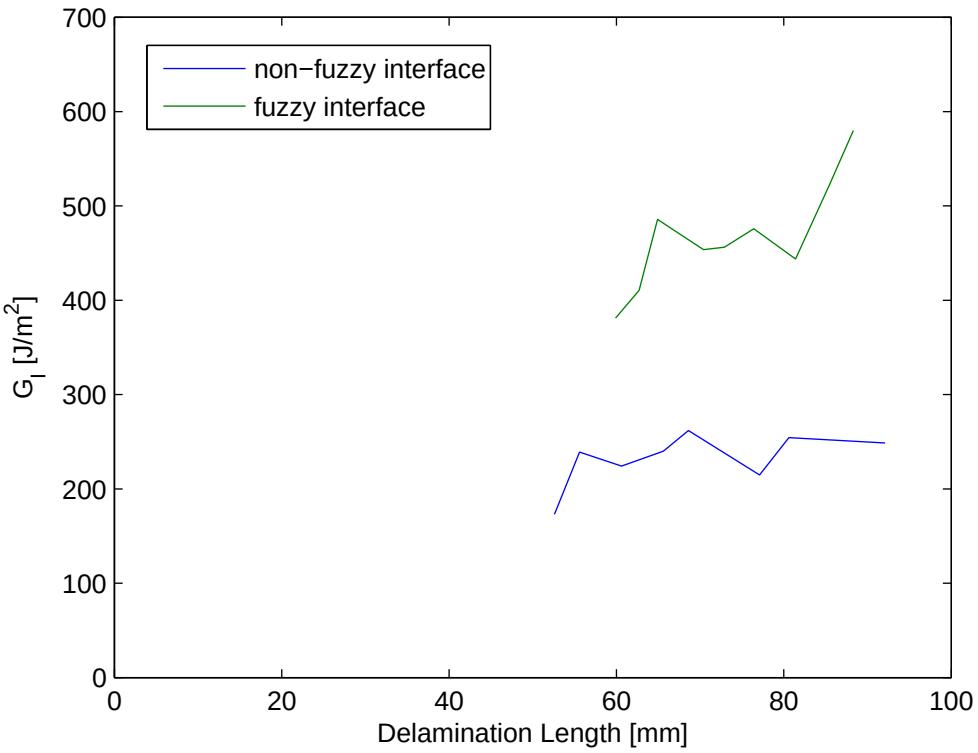


Figure 4.12: R-curve for fuzzy and non-fuzzy T650 specimens obtained experimentally

Finally, the effect of initial slope indicator is compared in Figure 4.13. As it is mentioned in [52], small values are taken for the initial slope indicator to provide numerical stability for the intrinsic cohesive zone model.It is seen that small variations of the initial slope constant does not affect the overall force vs. displacement response of the interface.

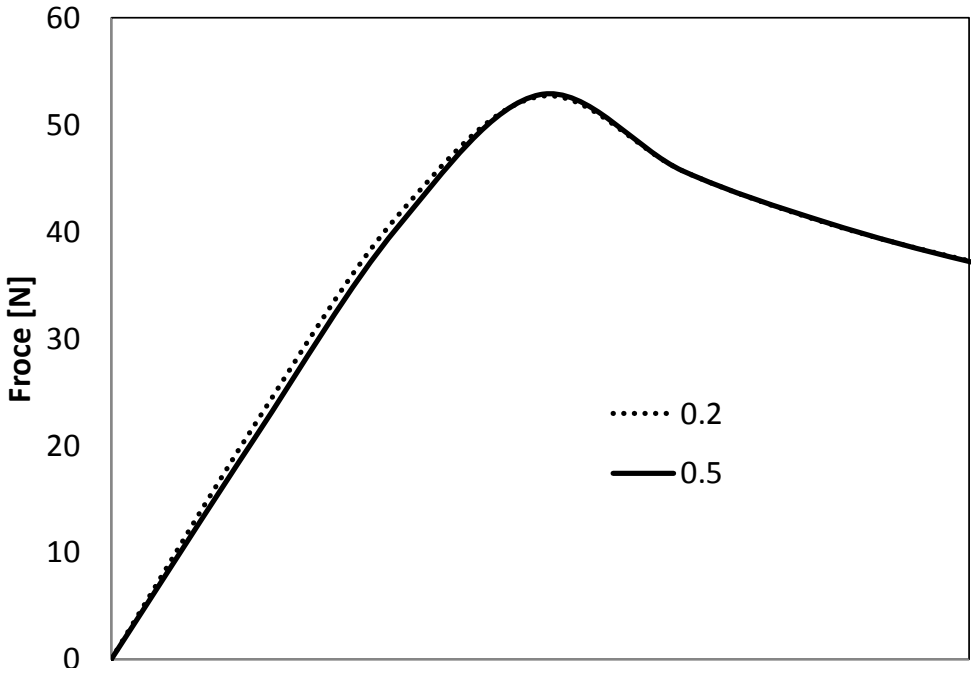


Figure 4.13: Effect of changing the shape parameter on the global force-displacement behavior

The cohesive zone parameters are calibrated in order to match the experimental results. The only interface property that can be obtained experimentally was $G_I$. An average value is taken with respect to the R-curve values, which is used as the fracture energy of the interface. One can obtain several sets of data to simulate the same behavior. However, the most effective cohesive zone properties are fracture energy and interface strength. By fixing one of them, prediction of the other property becomes easier. After the calibration of a set of these parameters, the examples analyzed are in good agreement with the test results. The results here are given for T650 PMC in Figures 4.14 and 4.15.

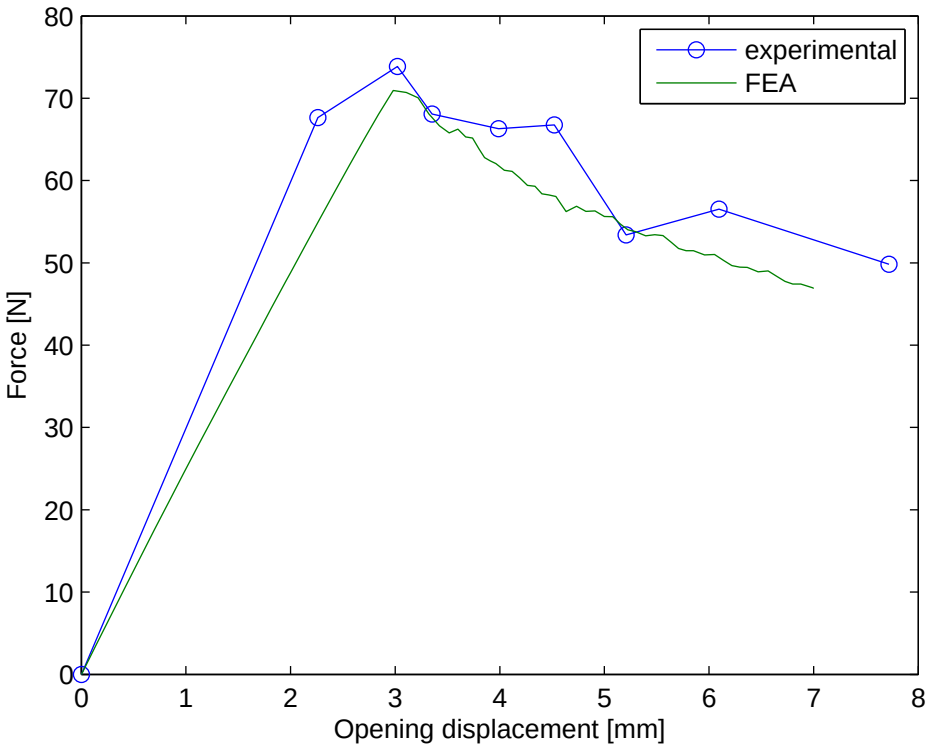


Figure 4.14: Experimental and FEA analysis for force vs. displacement for non-fuzzy T650 specimen

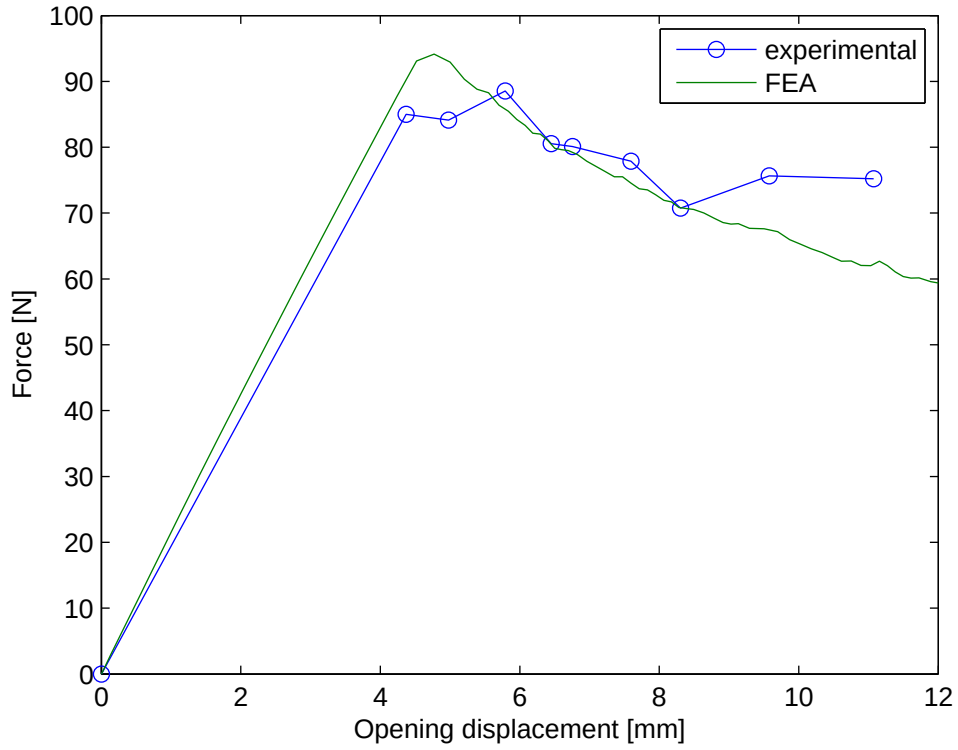


Figure 4.15: Experimental and FEA analysis for force vs. displacement for fuzzy T650 specimen

For the specimens with Ti-foil, the manufacturing process thermal residual stresses and high temperatures subjected during DCB test are considered, to analyze the crack initiation and propagation.

In Figure 4.16, the Von-Mises distribution is obtained as a contour plot. It can be seen that the section of the titanium layer connected to the bottom PMC layer (that is the region from the tip of the pre-crack to the end of the beam) in the specimen is under high tensional load. Then the specimen is placed in the oven at 110 C, which helps in relaxation of the thermal residual stresses. At this step, stresses are reduced to half of the initial stress state. Stresses in the opening direction

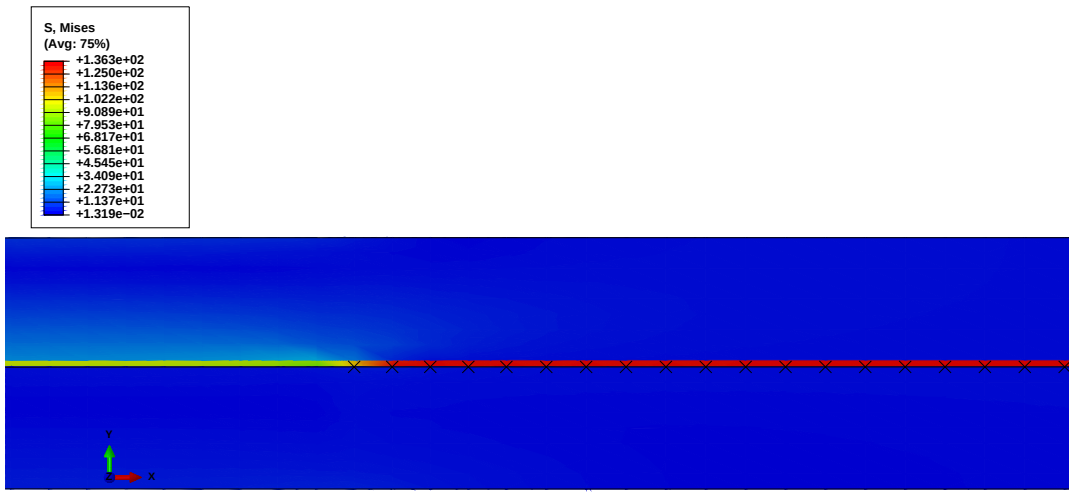


Figure 4.16: Thermal residual stresses developed after manufacturing of the DCB specimen with Ti-foil

(2-direction) are concentrated at the crack tip (Figures 4.17 and 4.18). The crack tip stress distribution is uneven caused by the asymmetry of the interface. When crack propagates, the asymmetry of the stresses increases and creates two major stress concentration regions at the interface,at the bottom and top surfaces of the interface. Meanwhile, the upper surface of titanium layer is in compression

Force vs. displacement curves for the DCB models at room and high temperature is given in Figure 4.19. The accumulated thermal stresses at the interface greatly affects the delamination process. Experimentally it is found that, at high temperatures,the interface has higher fracture energy (300-600 $J/m^2$).

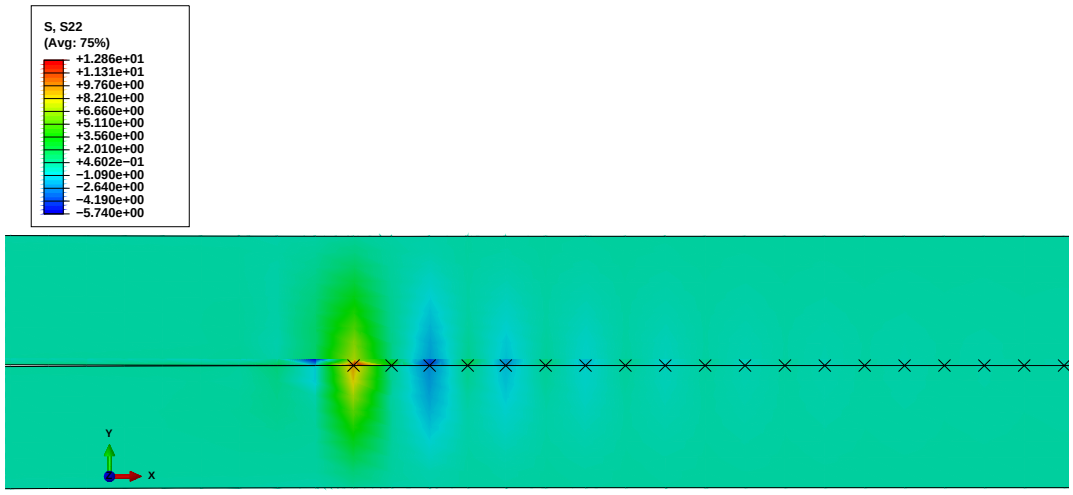


Figure 4.17: Thermal residual stress distribution around crack tip at high temperature test of the DCB specimen with Ti-foil before damage initiation

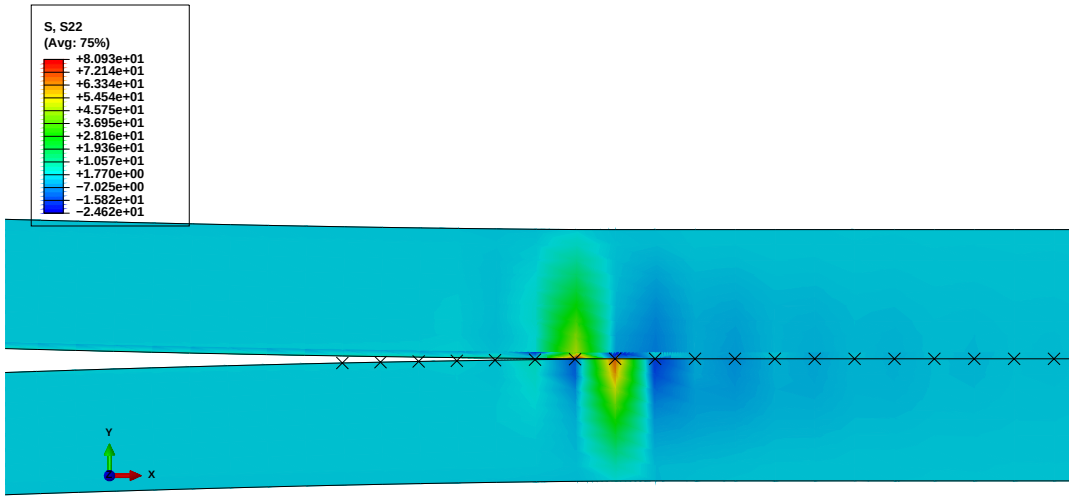


Figure 4.18: Stress distribution around crack tip at high temperature test of the DCB test model of a specimen with Ti-foil when crack propagates

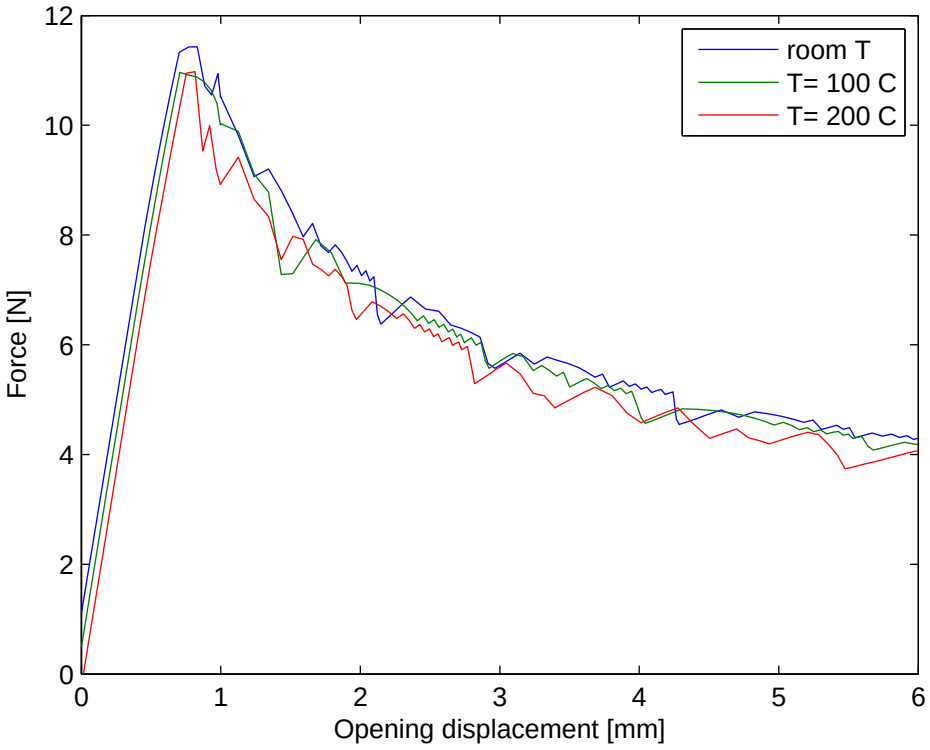


Figure 4.19: Comparison of the force vs. displacement curves for a DCB test model at different test temperatures

It is seen that the initial thermal residual stresses due to the manufacturing process increases the required force to initiate the crack. When the specimen is subjected to different temperature fields, some of the developing stresses are released by the thermal expansion of the materials. The force required to open the crack slightly lowers as temperature increases (Fig. 4.20).

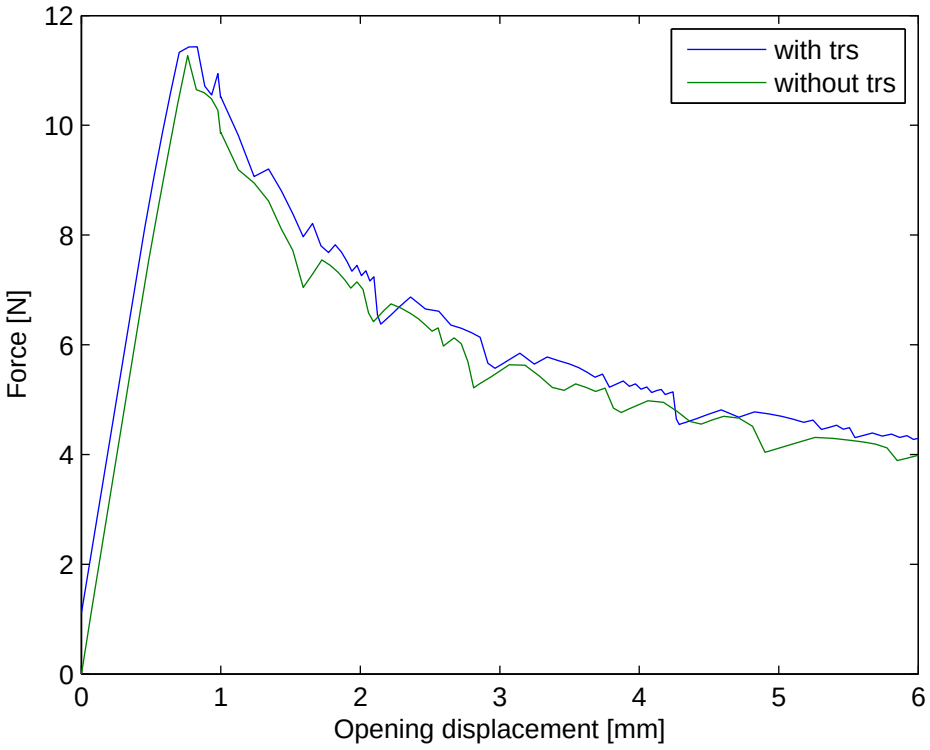


Figure 4.20: Comparison of the initial thermal residual stress (trs) effect on the delamination behavior

## 4.2 Single Lap Shear

A single lap shear test (ASTM D5868) serves to obtain the in-situ shear strength in adhesively bonded joints. The test is conducted by fixing one end of the specimen and pulling ate the other. However, due to eccentricity of the load, it not purely shear. The stress developed in the direction normal to the bond surface is called the peel stress. The stress distribution, concentration and its magnitude can be affected by the overlap length and adhesive layer thickness.

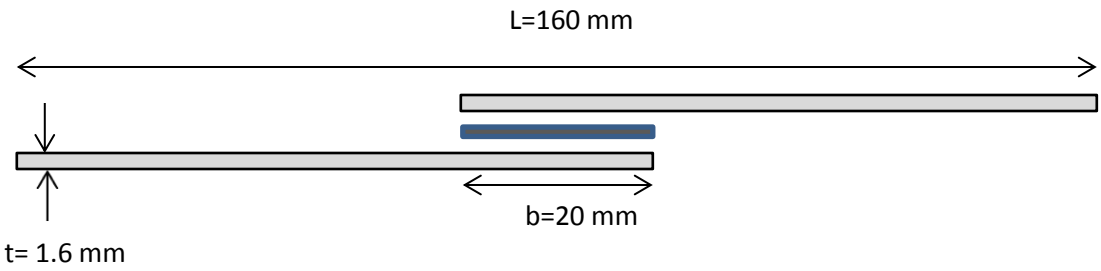


Figure 4.21: Geometry, boundary conditions, loading for the SLS joint model

A single lap shear model is developed to study the mixed mode cohesive zone at the interface and stress analysis under tensional load applied at its end. In this solution, both the adhesive and adherent layers are considered as isotropic elastic materials (Table 4.3). It is also assumed that the generalized plane stress condition

is valid, since the thicknesses of the adherents are much smaller than the other dimensions. Hence,the gradient of the stress through the thickness is neglected, and the shear force is transferred through the adhesive layer.

Table 4.3: Material properties of Ti and Skybond 700

| Material | Young's Modulus E (MPa) | Poisson's Ratio $\mu$ |
|---|---|---|
| Ti | 105000 | 0.37 |
| Skybond 700 | 1393 | 0.3 |

The length of the single lap joint is 160 cm, and the overlap region is 20 cm long. Both the upper and lower adherents are 1.6 mm thick. The adhesive layer are assumed finite thick. If it is assumed as a zero thickness layer, then the adhesive is modeled as a single row of cohesive elements, connecting the two adherents. If it is considered that it has a finite thickness then the adhesive layer is represented by continuum elements and there are two interfaces, i.e. upper interface between the upper adherent and the adhesive, and the lower interface between the lower adherent and the adhesive. These interfaces are then modeled as single row of cohesive elements. The geometry of the single lap shear model is shown in Figure 4.21. The joint is fixed at the left end and a tensional load is applied to the right end. Figure 4.22 shows the free body diagram, in which all the normal forces, shear forces and moments are shown.

In this SLS model, four node plain strain elements are used to model adherents and the adhesive, whereas 200 cohesive elements are placed along both the upper and lower interfaces between the adherents and the adhesive. The crack initiates at the free ends of the overlap region, since stress concentrations are observed close to the corners at these ends. Furthermore, the crack initiation occurs first at the

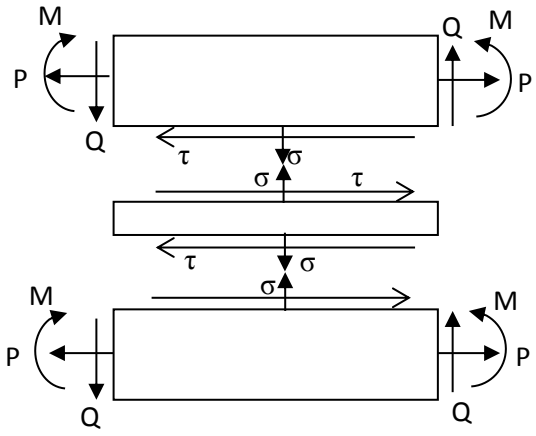


Figure 4.22: Free body diagram of the overlap region in a single lap shear

right end of the upper interface. This is the interface between the adhesive and the top adherent, at whose end the displacement boundary condition is applied. As mentioned earlier, clamped boundary condition is applied at the other end of the SLS specimen (bottom adherent). The dissimilar boundary conditions and the offset of the load due to SLS geometry causes slightly unsymmetrical stress distribution at the free ends of the overlap region. This can explain the non-simultaneous damage initiation and growth. Figure 4.23 is the right free end of the overlap region where damage initiated and the damage progressed.

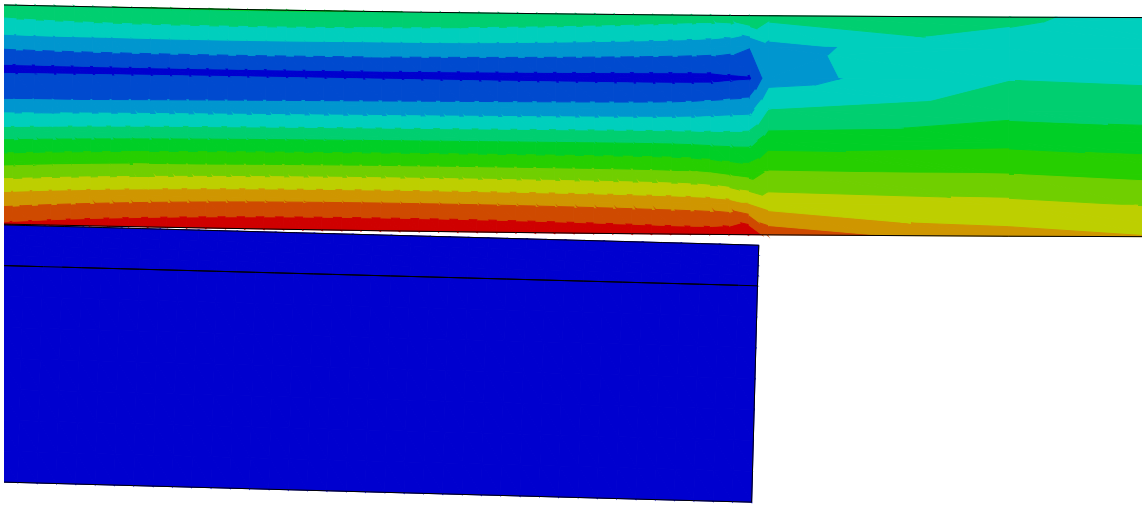

Figure 4.23: Right free end of the overlap region

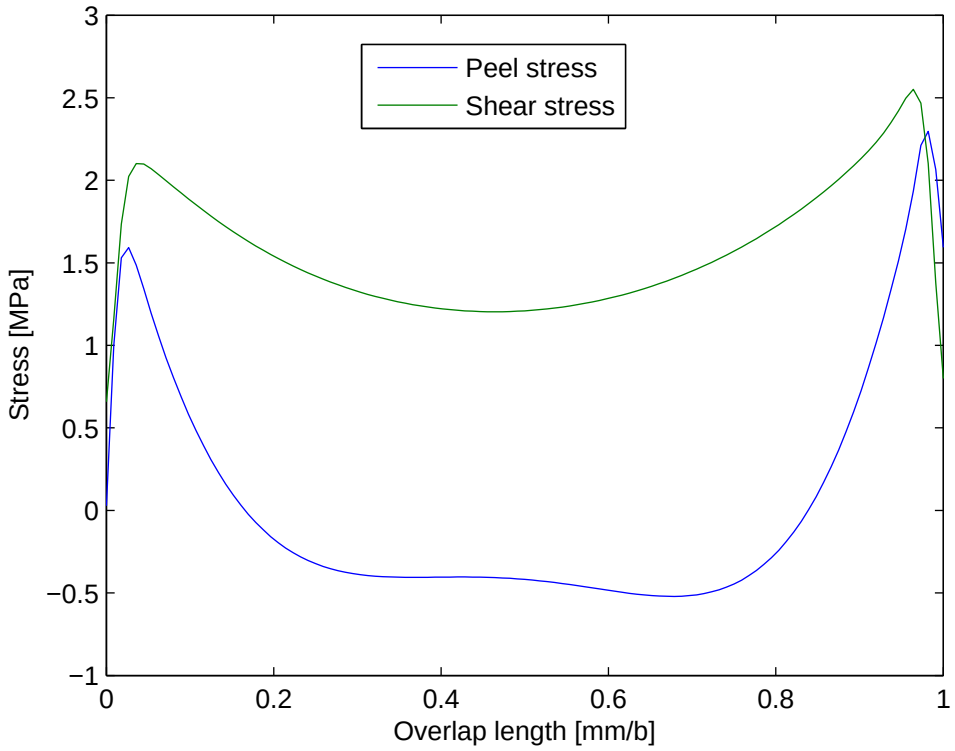




Figure 4.24: Free body diagram of the overlap region in a single lap shear

Figure 4.24 shows the shear and peel stress along the nondimensionalized overlap length. The stress values are taken just below the upper interface, when at damage initiation. This distribution of the stresses along the bond length is typical. The maximum values are close to the both ends, and decreasing toward the middle of the interface. The maximum values the peel and shear stress reach is higher at the right end.

The shear and peel stress distribution at crack propagation can be seen in Figure 4.25. As the cohesive elements continue to degrade, the crack propagates, and the peak of the stresses moves toward the middle of the overlap region. The increase in stresses is because the bonded area gets smaller, the stress per unit area increases.

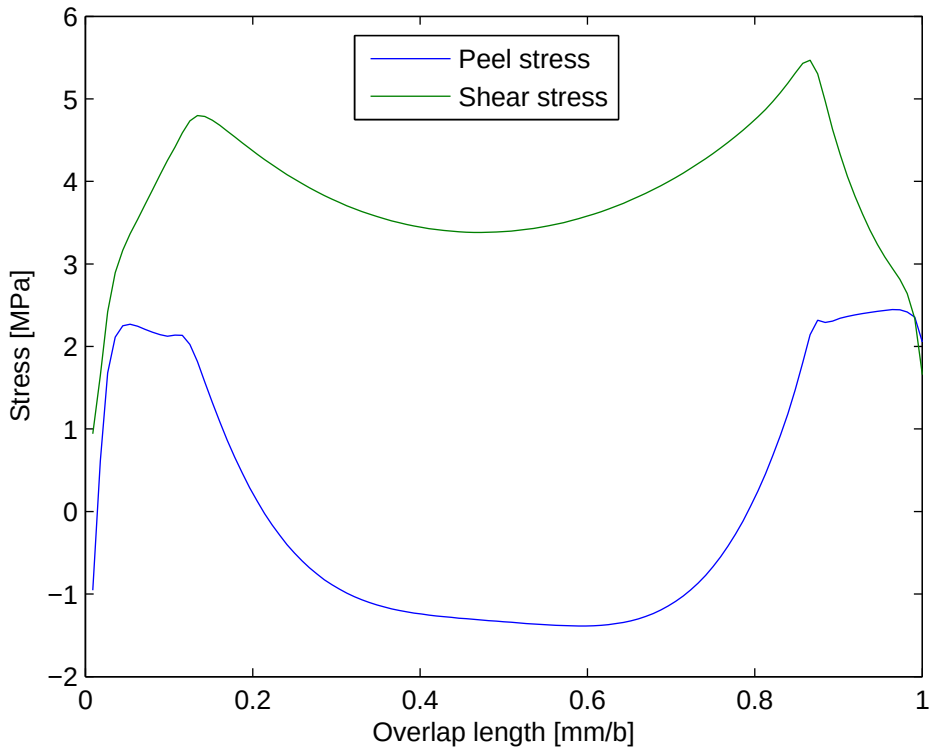


Figure 4.25: Free body diagram of the overlap region in a single lap shear

Shear and peel stress distributions are shown in Figures 4.26 and 4.27 for different temperatures ($T = 0, 150, 300°\mathrm{C}$) . A displacement control is applied at the right end of the specimen. As the temperature increases, the high stress values for both peel and shear reduce, whereas away from the free ends, temperature change is not much affective on shear and peel stress.

A similar trend was observed for viscoelastic adhesives in [69].

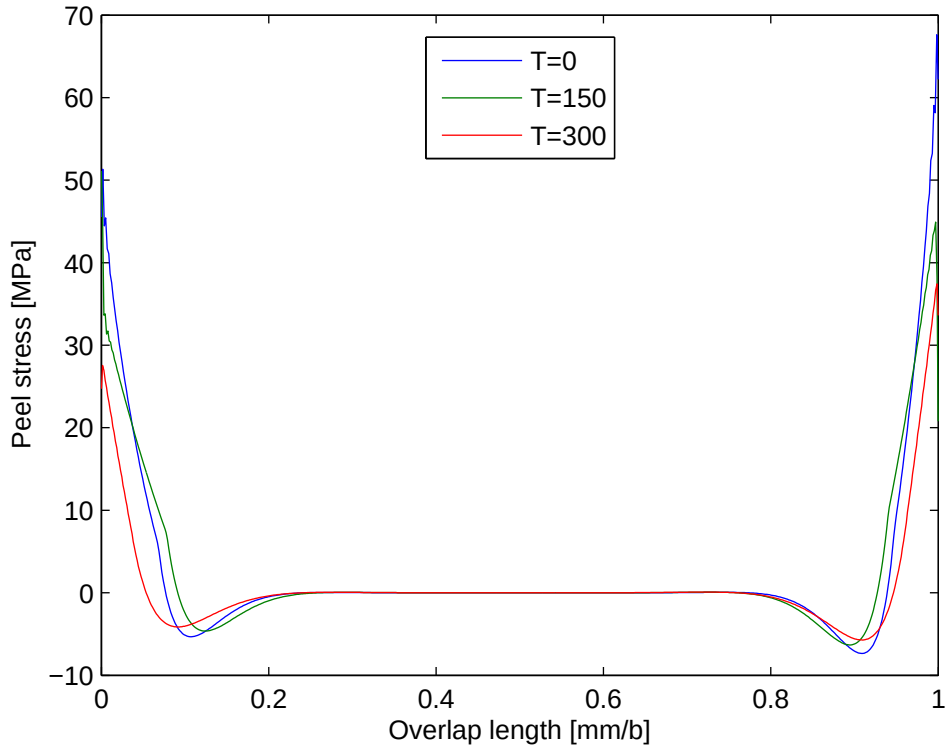


Figure 4.26: Peel stress distribution along the overlap length with respect to T

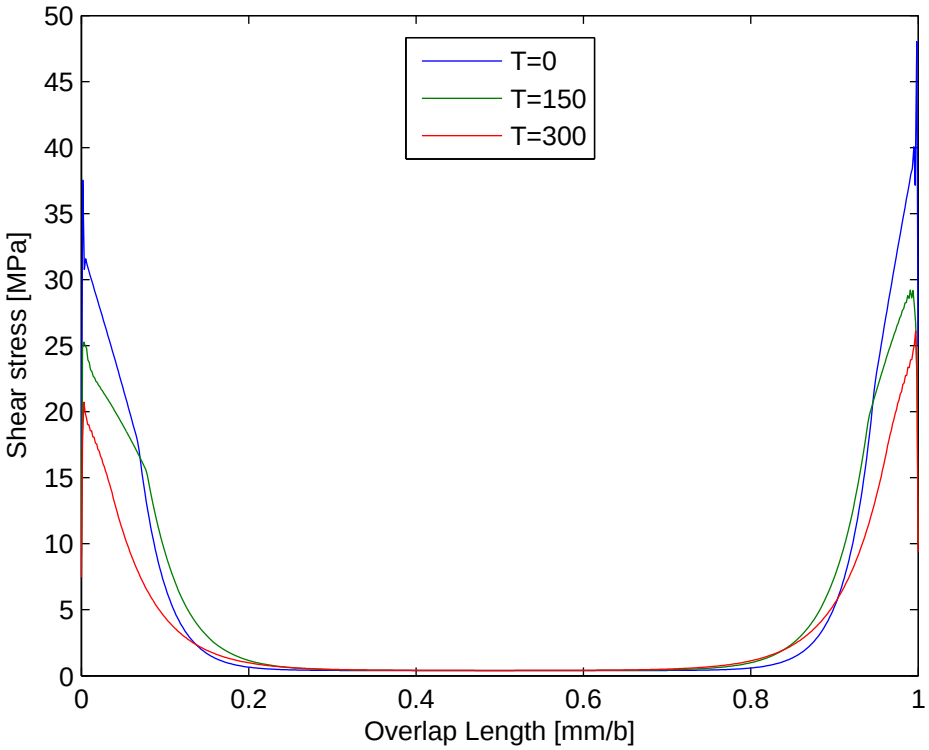


Figure 4.27: Shear stress distribution along the overlap length with respect to T

# 5. CONCLUSIONS

Nonlinear fracture process behavior at dissimilar material interfaces is investigated using a potential cohesive zone model. The cohesive zone model is utilized for quasi- static delamination and debonding problems. For computational simulation, two- dimensional four node cohesive elements are used to analyze the interfaces in PMCs, PMC/metal and adhesively bonded joints.

A computational model is developed to study delaminations in laminated composite plates subjected to mechanical and thermal loads, as well as to design and predict the thermomechanical interface response. The model incorporates extreme environment conditions such as high temperature. Different interfaces in PMC/PMC, metal/PMC joints, are examined using a potential-based cohesive zone theory. The potential based CZM theory contains eight fracture parameters. these parameters can be estimated through micromechanics and experimental studies. Estimating these parameters are challenging, and one can get many set of parameters for an interface. Required parameters can be estimated by matching with the relative experimental data, by fixing the parameters obtained experimentally or analytically. Hence, a parametric study is essential for a better understanding of the effects of the cohesive zone parameters.

The DCB and SLS simulations are conducted to predict the properties of interfaces and damage initiation and stress distributions along the crack paths. address the effect of various cohesive zone properties.

- A potential-based model is studied, which identifies different fracture energies and cohesive strength in each fracture mode. The model can be applied to a wide range of material systems..

- Determination of the cohesive zone parameters is very challenging, as well as very important in order to get better results. For this purpose, several parametric analysis are conducted to identify the effect of the cohesive zone parameters, which have a dominant effect on results.

- Thermal residual stress is a significant concern for composite materials. Residual stresses can initially develop by both chemical shrinkage of the resin and CTE mismatch. Structures operating in hostile environments are subjected to high temperatures. Effects of the mentioned sources of stresses are taken into account in models. Therefore, the models provide a better understanding of how the failure initiation and propagation are affected when there is thermal loading.

- An extension is suggested for the existing potential-based model for the frictional relationships during contact of newly created surfaces. It can utilize the Coulomb friction, which may exist in mode II dominant cases. Herein it is shown only analytically, but the frictional constitutive relationship can be integrated with any potential-based model.

- A correction is proposed analytically, to add thermal expansion effects in the interface. Since thermal expansion causes the interface to open, it can be related to crack openings to be able to show the effect of both the thermal and mechanical loading.

It is worth noting that the cohesive zone model can be successfully used to de-

scribe many fracture processes in a wide range of material systems. With the aim of obtaining better predictions, however, carefully designed, and conducted experiments play an important role to extract the required cohesive zone parameters. Furthermore, a fatigue crack model is necessary to investigate long term cyclic thermal and mechanical loadings.

# REFERENCES


[1] D.S. Dugdale. Yielding of steel sheets containing slits. *Journal of the Mechanics and Physics of Solids*, 8(2):100–104, 1960.

[2] G.I. Barenblatt. The mathematical theory of equilibrium cracks in brittle fracture. *Advances in applied mechanics*, 7(1):55–129, 1962.

[3] G.I. Barenblatt. The formation of equilibrium cracks during brittle fracture. general ideas and hypotheses. axially-symmetric cracks. *Journal of Applied Mathematics and Mechanics*, 23(3):622–636, 1959.

[4] F. Erdogan. On the crack extension in plates under plane loading and transverse shear. *Journal of Basic Engineering*, 85(4):519, 1963.

[5] G.P. Anderson, V.L. Ruggles, and G.S. Stibor. Use of finite element computer programs in fracture mechanics. *International Journal of Fracture Mechanics*, 7(1):63–76, 1971.

[6] G.C. Sih. Strain-energy-density factor applied to mixed mode crack problems. *International Journal of Fracture*, 10(3):305–321, 1974.

[7] R. Hill. Acceleration waves in solids. *Journal of the Mechanics and Physics of Solids*, 10(1):1–16, 1962.

[8] G.T. Camacho and M. Ortiz. Computational modelling of impact damage in brittle materials. *International Journal of Solids and Structures*, 33(20):2899–2938, 1996.

[9] V. Tvergaard and J. W. Hutchinson. The relation between crack growth resistance and fracture process parameters in elastic-plastic solids. *Journal of the Mechanics and Physics of Solids*, 40(6):1377–1397, 1992.

[10] M.J. Van den Bosch, P.J.G. Schreurs, and M.G.D. Geers. An improved description of the exponential xu and needleman cohesive zone law for mixed-mode decohesion. *Engineering Fracture Mechanics*, 73(9):1220–1234, 2006.

[11] X.-P. Xu and A. Needleman. Void nucleation by inclusion debonding in a crystal matrix. *Modelling and Simulation in Materials Science and Engineering*, 1(2):111, 1993.

[12] M. Ortiz and A. Pandolfi. Finite-deformation irreversible cohesive elements for three-dimensional crack-propagation analysis. *International Journal for Numerical Methods in Engineering*, 44(9):1267–1282, 1999.

[13] N. Chandra, Shet C. Li, H., and H. Ghonem. Some issues in the application of cohesive zone models for metal–ceramic interfaces. *International Journal of Solids and Structures*, 39(10):2827–2855, 2002.

[14] A. Needleman. A continuum model for void nucleation by inclusion debonding. *Journal of Applied Mechanics*, 54(3):525–531, 1987.

[15] V. Tvergaard and J.W. Hutchinson. The influence of plasticity on mixed mode interface toughness. *Journal of the Mechanics and Physics of Solids*, 41(6):1119–1135, 1993.

[16] P.H. Geubelle and J.S. Baylor. Impact-induced delamination of composites: a 2d simulation. *Composites Part B: Engineering*, 29(5):589–602, 1998.

[17] Q.D. Yang and M.D. Thouless. Mixed-mode fracture analyses of plastically-deforming adhesive joints. *International Journal of Fracture*, 110(2):175–187, 2001.

[18] P.P. Camanho and C.G. Dávila. Mixed-mode decohesion finite elements for the simulation of delamination in composite materials. *NASA-Technical Paper*,

211737(1):33, 2002.

[19] Z.J. Zhang and G.H. Paulino. Cohesive zone modeling of dynamic failure in homogeneous and functionally graded materials. *International Journal of Plasticity*, 21(6):1195–1254, 2005.

[20] M.G. Kulkarni, P.H. Geubelle, and K. Matouš. Multi-scale modeling of heterogeneous adhesives: Effect of particle decohesion. *Mechanics of Materials*, 41(5):573–583, 2009.

[21] M.G. Kulkarni, K. Matouš, and P.H. Geubelle. Coupled multi-scale cohesive modeling of failure in heterogeneous adhesives. *International Journal for Numerical Methods in Engineering*, 84(8):916–946, 2010.

[22] K. Matouš, M.G. Kulkarni, and P.H. Geubelle. Multiscale cohesive failure modeling of heterogeneous adhesives. *Journal of the Mechanics and Physics of Solids*, 56(4):1511–1533, 2008.

[23] A. Needleman. An analysis of tensile decohesion along an interface. *Journal of the Mechanics and Physics of Solids*, 38(3):289–324, 1990.

[24] L. Banks-Sills and Y. Bortman. A mixed-mode fracture specimen: analysis and testing. *International Journal of Fracture*, 30(3):181–201, 1986.

[25] J.R. Reeder and J.H. Rews. Mixed-mode bending method for delamination testing. *AiAA Journal*, 28(7):1270–1276, 1990.

[26] M.L. Benzeggagh and M. Kenane. Measurement of mixed-mode delamination fracture toughness of unidirectional glass/epoxy composites with mixed-mode bending apparatus. *Composites Science and Technology*, 56(4):439–449, 1996.

[27] J.H. Rose, J. Ferrante, and J.R. Smith. Universal binding energy curves for metals and bimetallic interfaces. *Physical Review Letters*, 47:675–678, 1981.

[28] J.R. Rice. Dislocation nucleation from a crack tip: an analysis based on the peierls concept. *Journal of the Mechanics and Physics of Solids*, 40(2):239–271, 1992.

[29] M.E. Gurtin. Thermodynamics and the cohesive zone in fracture. *Zeitschrift für angewandte Mathematik und Physik ZAMP*, 30(6):991–1003, 1979.

[30] M. Fagerström and R. Larsson. A thermo-mechanical cohesive zone formulation for ductile fracture. *Journal of the Mechanics and Physics of Solids*, 56(10):3037–3058, 2008.

[31] A. Hattiangadi and T. Siegmund. A thermomechanical cohesive zone model for bridged delamination cracks. *Journal of the Mechanics and Physics of Solids*, 52(3):533–566, 2004.

[32] L. Benabou, Z. Sun, and P.-R. Dahoo. A thermo-mechanical cohesive zone model for solder joint lifetime prediction. *International Journal of Fatigue*, 49:18–30, 2013.

[33] G. Nikolova and J. Ivanova. Cracked bi-material plates under thermomechanical loading. *Key Engineering Materials*, 409:406–413, 2009.

[34] P. Hu, X. Han, L.F.M. da Silva, and W.D. Li. Strength prediction of adhesively bonded joints under cyclic thermal loading using a cohesive zone model. *International Journal of Adhesion and Adhesives*, 41:6–15, 2013.

[35] M. Goland and E. Reissner. The stresses in cemented joints. *Journal of Applied Mechanics*, 11(1):A17–A27, 1944.

[36] R.D. Adams and N.A. Peppiatt. Stress analysis of adhesive-bonded lap joints. *The Journal of Strain Analysis for Engineering Design*, 9(3):185–196, 1974.

[37] I.U. Ojalvo and H.L. Eidinoff. Bond thickness effects upon stresses in single-lap adhesive joints. *AIAA Journal*, 16(3):204–211, 1978.

[38] W.C. Carpenter. Stresses in bonded connections using finite elements. *International Journal for Numerical Methods in Engineering*, 15:1659–1680, 1980.

[39] J.N. Reddy and S. Roy. Non-linear analysis of adhesively bonded joints. *International Journal of Non-linear Mechanics*, 23(2):97–112, 1988.

[40] B. Zhao and Z.-H. Lu. A two-dimensional approach of single-lap adhesive bonded joints. *Mechanics of Advanced Materials and Structures*, 16(2):130–159, 2009.

[41] B. Zhao, Z.-H. Lu, and Y.-N. Lu. Closed-form solutions for elastic stress–strain analysis in unbalanced adhesive single-lap joints considering adherend deformations and bond thickness. *International Journal of Adhesion and Adhesives*, 31(6):434–445, 2011.

[42] D.A. Bigwood and A.D. Crocombe. Elastic analysis and engineering design formulae for bonded joints. *International journal of Adhesion and Adhesives*, 9(4):229–242, 1989.

[43] A.G. Magalhães, M.F.S.F. De Moura, and J.P.M. Gonçalves. Evaluation of stress concentration effects in single-lap bonded joints of laminate composite materials. *International Journal of Adhesion and Adhesives*, 25(4):313–319, 2005.

[44] C. Yang, H. Huang, J.S. Tomblin, and W. Sun. Elastic-plastic model of adhesive-bonded single-lap composite joints. *Journal of Composite Materials*, 38(4):293–309, 2004.

[45] P.A. Cooper and J.W. Sawyer. A critical examination of stresses in an elastic single lap joint. Technical report, DTIC Document, 1979.

[46] F. Delale, F. Erdogan, and M.N. Aydinoglu. Stresses in adhesively bonded joints: a closed-form solution. *Journal of Composite Materials*, 15(3):249–271, 1981.

[47] G. Li, P. Lee-Sullivan, and R.W. Thring. Nonlinear finite element analysis of stress and strain distributions across the adhesive thickness in composite single-lap joints. *Composite Structures*, 46(4):395–403, 1999.

[48] G. Alfano and M.A. Crisfield. Finite element interface models for the delamination analysis of laminated composites: mechanical and computational issues. *International Journal for Numerical Methods in Engineering*, 50(7):1701–1736, 2001.

[49] M.F.S.F. De Moura, J.P.M. Gonçalves, J.A.G. Chousal, and R.D.S.G. Campilho. Cohesive and continuum mixed-mode damage models applied to the simulation of the mechanical behaviour of bonded joints. *International Journal of Adhesion and Adhesives*, 28(8):419–426, 2008.

[50] D. Xie and A.M. Waas. Discrete cohesive zone model for mixed-mode fracture using finite element analysis. *Engineering Fracture Mechanics*, 73(13):1783–1796, 2006.

[51] K.L. Roe and T. Siegmund. An irreversible cohesive zone model for interface fatigue crack growth simulation. *Engineering Fracture Mechanics*, 70(2):209–232, 2003.

[52] M.F.S.F. De Moura and J.A.G. Chousal. Cohesive and continuum damage models applied to fracture characterization of bonded joints. *International Journal of Mechanical Sciences*, 48(5):493–503, 2006.

[53] R. Tenchev and B. Falzon. Experimental and numerical study of debonding in composite adhesive joints. In *International Conference on Composite Materials (Proceedings), Kyoto, Japan, July*, pages 8–13, 2007.

[54] Y. Mi, M.A. Crisfield, G.A.O. Davies, and H.B. Hellweg. Progressive delamination using interface elements. *Journal of Composite Materials*, 32(14):1246–1272, 1998.

[55] Paul W.H. and Stephen R.H. Cohesive zone length in numerical simulations of composite delamination. *Engineering Fracture Mechanics*, 75(16):4774 – 4792, 2008.

[56] S.T. Pinho, L. Iannucci, and P. Robinson. Formulation and implementation of decohesion elements in an explicit finite element code. *Composites Part A: Applied science and manufacturing*, 37(5):778–789, 2006.

[57] A. Turon, P.P. Camanho, J. Costa, and C.G. Dávila. A damage model for the simulation of delamination in advanced composites under variable-mode loading. *Mechanics of Materials*, 38(11):1072–1089, 2006.

[58] A. Turon, C.G. Davila, P.P. Camanho, and J. Costa. An engineering solution for mesh size effects in the simulation of delamination using cohesive zone models. *Engineering Fracture Mechanics*, 74(10):1665–1682, 2007.

[59] T. Diehl. On using a penalty-based cohesive-zone finite element approach, part i: Elastic solution benchmarks. *International Journal of Adhesion and Adhesives*, 28(4):237–255, 2008.

[60] T. Diehl. On using a penalty-based cohesive-zone finite element approach, part ii: Inelastic peeling of an epoxy-bonded aluminum strip. *International Journal of Adhesion and Adhesives*, 28(4):256–265, 2008.

[61] V.K. Goyal, E.R. Johnson, and V.K. Goyal. Predictive strength-fracture model for composite bonded joints. *Composite Structures*, 82(3):434–446, 2008.

[62] K. Park and G.H. Paulino. Computational implementation of the ppr potential-based cohesive model in abaqus: Educational perspective. *Engineering Fracture Mechanics*, 93:239–262, 2012.

[63] K. Park, G.H. Paulino, and J.R. Roesler. A unified potential-based cohesive model of mixed-mode fracture. *Journal of the Mechanics and Physics of Solids*, 57(6):891–908, 2009.

[64] K. Park. *Potential-based fracture mechanics using cohesive zone and virtual internal bond modeling*. PhD thesis, University of Illinois at Urbana-Champaign, 2010.

[65] G. Lin, P.H. Geubelle, and N.R. Sottos. Simulation of fiber debonding with friction in a model composite pushout test. *International Journal of Solids and Structures*, 38(46):8547–8562, 2001.

[66] I. Özdemir, W.A.M. Brekelmans, and M.G.D. Geers. A thermo-mechanical cohesive zone model. *Computational Mechanics*, 46(5):735–745, 2010.

[67] D.A. Burianek, A.E. Giannakopoulos, and S.M. Spearing. Modeling of facesheet crack growth in titanium–graphite hybrid laminates, part i. *Engineering Fracture Mechanics*, 70(6):775–798, 2003.

[68] D.A. Burianek and S.M. Spearing. Modeling of facesheet crack growth in titanium–graphite hybrid laminates, part ii: Experimental results. *Engineering Fracture Mechanics*, 70(6):799–812, 2003.

[69] F. Cheng, Ö. Ö. Özsoy, and J.N. Reddy. Finite element modeling of viscoelastic behavior and interface damage in adhesively bonded joints. In S. Kumar and

K.L. Mittal, editors, *Advances in Modeling and Design of Adhesively Bonded Systems*, pages 23–47. Scrivener Publishing LLC and Wiley & Sons, Inc., New Jersey and Massachusetts.